

This article appeared in a journal published by Elsevier. The attached copy is furnished to the author for internal non-commercial research and education use, including for instruction at the authors institution and sharing with colleagues.

Other uses, including reproduction and distribution, or selling or licensing copies, or posting to personal, institutional or third party websites are prohibited.

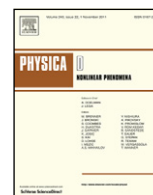
In most cases authors are permitted to post their version of the article (e.g. in Word or Tex form) to their personal website or institutional repository. Authors requiring further information regarding Elsevier's archiving and manuscript policies are encouraged to visit:

<http://www.elsevier.com/copyright>



Contents lists available at SciVerse ScienceDirect

Physica D

journal homepage: www.elsevier.com/locate/physd

Pattern solutions of the Klausmeier model for banded vegetation in semi-arid environments III: The transition between homoclinic solutions

Jonathan A. Sherratt*

Department of Mathematics and Maxwell Institute for Mathematical Sciences, Heriot-Watt University, Edinburgh EH14 4AS, UK

ARTICLE INFO

Article history:

Received 14 March 2011

Received in revised form

15 November 2011

Accepted 18 August 2012

Available online 24 August 2012

Communicated by Y. Nishiura

Keywords:

Pattern formation

Homoclinic

Mathematical model

Brousse tigrée

Perturbation theory

Limit cycle

Reaction–diffusion advection

ABSTRACT

Self-organised patterns of vegetation are a characteristic feature of semi-deserts. On hillsides, these typically comprise vegetation bands running parallel to the contours, separated by regions of bare ground (“tiger bush”). The present study concerns the Klausmeier mathematical model for this phenomenon [C.A. Klausmeier, Regular and irregular patterns in semiarid vegetation, *Science* 284 (1999) 1826–1828], which is one of the earliest and most influential of the various theoretical models for banded vegetation. The model is a system of reaction–diffusion–advection equations, and after rescaling it contains three dimensionless parameters, one of which (the slope parameter) is much larger than the other two. The present study is the third in a series of papers in which the author exploits the large value of the slope parameter to obtain leading order approximations to the parameter regions in which patterns exist, and to the form of these patterns. The boundary of the parameter region giving patterns consists in part of two loci of homoclinic solutions, that are homoclinic to different steady states. The present paper concerns behaviour for parameters close to the intersection point of these loci. The author shows that this part of parameter space divides naturally into three regions, with a different solution structure in each. In one region, the solution corresponds to a limit cycle of a reduced system of ordinary differential equations; the other two regions involve multiple matched layers. As part of the analysis, the author derives formulae for the homoclinic solution loci, and for the location of their intersection. All of the results are valid to leading order for large values of the slope parameter. The author presents a detailed numerical verification of his analytical results. The paper concludes with discussions of the ecological implications of the results, and the main outstanding mathematical questions.

© 2012 Published by Elsevier B.V.

1. Introduction

Self-organised patterns of vegetation are a characteristic feature of semi-deserts. The most striking and best studied example is striped patterns on gentle slopes (see [1,2] for a review). These occur in many parts of the world, and are particularly well documented in Australia [3,4], Mexico/South-Western USA [5,6] and sub-Saharan Africa [7–9]. Bands of grass, shrubs or trees run along contours, separated by bare ground; wavelengths of about 1 km are typical for trees and shrubs, with shorter wavelengths observed for grasses.

Field studies of banded vegetation are difficult and expensive because of poor infrastructure near potential study sites. Moreover vegetation bands have never been generated successfully in a laboratory setting, and the slow timescale of pattern evolution (decades) makes observational data of limited use for investigating the implications of environmental changes such as altered levels of rainfall. Therefore a number of authors have used theoretical

models to study banded vegetation (reviewed in [10]). One influential modelling approach has been led by Lefever and co-workers (e.g. [11–14]), and is based on the different length scales of the tree/shrub crowns and root systems. These models exhibit pattern formation via short range activation and long range inhibition. The other major class of models is based on water redistribution. The first studies of this type used cellular automata [15–17]. A shift to partial differential equations as the main modelling tool was initiated by Klausmeier [18], and his model is the subject of this paper. When suitably nondimensionalised [18,19], the equations are

$$\frac{\partial u}{\partial t} = \overbrace{wu^2}^{\text{plant growth}} - \overbrace{Bu}^{\text{plant loss}} + \overbrace{\partial^2 u / \partial x^2}^{\text{plant dispersal}} \quad (1a)$$

$$\frac{\partial w}{\partial t} = \underbrace{A}_{\text{rainfall}} - \underbrace{w}_{\text{evaporation}} - \underbrace{wu^2}_{\text{uptake by plants}} + \underbrace{v \partial w / \partial x}_{\text{flow downhill}} \quad (1b)$$

Here $u(x, t)$ is plant density, $w(x, t)$ is water density, t is time and x is a one-dimensional space variable running in the uphill direction. Although they represent a combination of ecological quantities, the

* Tel.: +44 131 451 3249; fax: +44 131 451 3249.

E-mail address: jas@ma.hw.ac.uk.

(dimensionless) parameters A , B and ν can be most usefully interpreted as reflecting rainfall, plant loss and slope gradient respectively. Note that (1) assumes that the slope is constant. A variant of (1) with a spatially varying slope parameter, consisting of small oscillations about zero, was used by Klausmeier [18] to study two-dimensional mosaic patterns of vegetation on (approximately) flat ground.

Klausmeier's equations (1) were the first of a large number of partial differential equation models for patterning due to water redistribution (e.g. [20–32]). Taken together, these studies have had a major impact on the current understanding of banded vegetation. However, in all cases the authors have relied on numerical simulations of their equations, with little or no underlying analytical theory. Even for (1), previous analysis does not extend beyond linear stability of spatially homogeneous solutions [18,19]. This paper is the third in a series whose objective is a detailed analytical understanding of pattern solutions of the Klausmeier model (1).

The advection term in (1b) means that spatial patterns are not stationary; rather they move in the positive x direction (uphill) at a constant rate. There has been a long-running debate in the ecological literature about this uphill migration, with some field studies reporting stationary patterns (e.g. [3]). However, the majority of data sets spanning a time period sufficient to address this issue do indicate uphill migration, with speeds in the range $0.2\text{--}1\text{ m year}^{-1}$ (see Table 5 of [1]). Moreover, a recent and very detailed study using photographic data from satellites [33, Chapter 10] confirms migration, with speeds in this range, for three different geographical locations. The ecological cause of uphill migration is that moisture levels are higher on the uphill edge of the bands than on their downhill edge, leading to reduced plant death and greater seedling density [34,35].

Since they move at a constant speed, pattern solutions of (1) are periodic travelling waves (wavetrains), with the mathematical form $u(x, t) = U(z)$, $w(x, t) = W(z)$. Here $z = x - ct$, with $c > 0$ being the migration speed. Substituting these solution forms into (1) gives

$$d^2U/dz^2 + c dU/dz + WU^2 - BU = 0 \quad (2a)$$

$$(\nu + c)dW/dz + A - W - WU^2 = 0. \quad (2b)$$

Patterns correspond to periodic solutions of (2), and in the many simulation-based studies of (1) (e.g. [18,19,36]) such patterns are the only non-constant solutions that have been found at large times.¹ Previously, Gabriel Lord and I used numerical bifurcation analysis to study these periodic solutions [37]. We showed that for a given value of the migration speed c , patterns occur for a range of values of the rainfall parameter A . Fig. 1 shows a typical example of the part of the A – c parameter plane in which patterns occur. The thick curve at the upper end of the rainfall range giving patterns is the locus of a Hopf bifurcation point in (2), while the thin curves are the loci of homoclinic solutions.

Note that the parameter region giving patterns extends significantly above $c = 18$, which is the upper limit in Fig. 1. For some larger values of c , the lower end of the rainfall range giving patterns consists of the locus of a fold in the pattern solution branch, rather than the locus of a homoclinic solution [38]; however this is not relevant to the behaviour considered in this paper. Intuitively, spatially uniform vegetation occurs at high levels of rainfall, and no

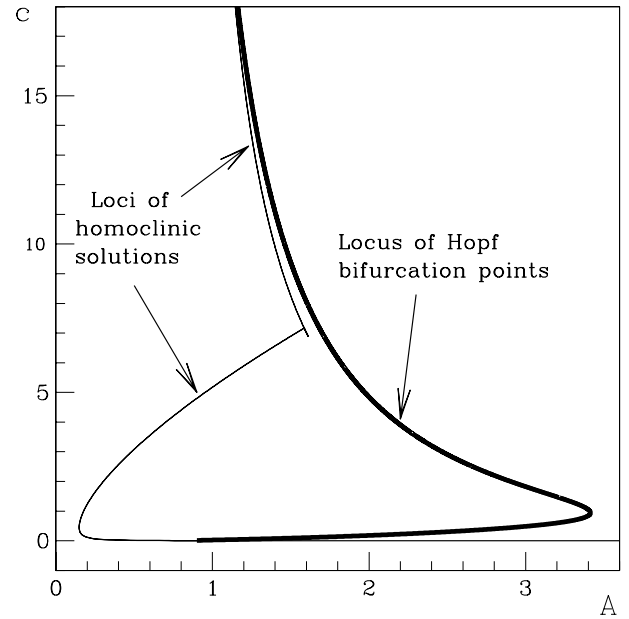


Fig. 1. An illustration of the region in the A – c parameter plane in which there are patterned solutions of (1). The thick curve is the locus of Hopf bifurcation points of (2) and the thin curves are the loci of homoclinic solutions. These curves bound the illustrated part of the pattern region. The plot is truncated at $c \approx 20$. Patterns actually exist for values of c up to about 54, and details of patterns for these larger values of c are given in [38]. The numerical solutions were performed using AUTO [39–41]; see [37] for further details. Note that I have not attempted to calculate the loci of actual homoclinic solutions; rather the thin curves are loci of periodic solutions of a fixed but very long wavelength (2000). The case shown is for $B = 0.45$ and $\nu = 200$.

vegetation is possible when rainfall is very low. Intermediate rainfall levels cannot sustain uniform vegetation, but patterned vegetation is possible.

The parameters A , B and ν depend on both the type of vegetation and the physical environment. The rainfall parameter A can take values between about 0.1 and 3.0 [18,22], and estimates of the plant loss parameter B lie in the range 0.05–2.0 [18,22]. In comparison the slope parameter ν is much larger: Klausmeier [18] estimated its value at 182.5. This large value is not due to the slope itself being steep: banded vegetation is restricted to slopes of a few per cent, and on steeper slopes, different processes occur because rainwater generates gullies. Rather, ν is large because the plant diffusion coefficient is small compared to the advection rate of water, and it is the relative values of these quantities that determines the nondimensional parameter ν [18,19]. Mathematically, the large value of ν suggests an investigation of the asymptotic form of periodic solutions of (2). This paper is the third in a series in which I take this approach. My objective is to study the boundaries of parameter space in which patterns occur, and the form of these patterns, for large ν . Previously [38,42] I have studied the “tusk-shaped” region that occurs for c greater than about 7 in Fig. 1. I showed that this region occurs when $\nu^{1/2} \ll c \ll \nu$ and $A^2c = O_s(\nu)$; here I use the notation $f = O_s(g)$ to mean that $f = O(g)$ and $f \neq o(g)$. This previous work involved a series of rescalings of the travelling wave equations (2) that yield the leading order equations satisfied by pattern solutions in the “tusk-shaped” region. One of the implications of this work was that the rescalings broke down when $c = O(\nu^{1/2})$; in that case the range of rainfall levels giving patterns is much wider. In this paper I study the specific case of $c = O_s(\nu^{1/2})$ and $A = O_s(\nu^{1/4})$. This is a rather localised part of the A – c parameter plane, but it is a particularly interesting and important region, containing a fundamental shift in pattern form. Of special note is that the thin curve in Fig. 1 is actually the loci of two different homoclinic solutions, which are

¹ I mention in Section 2 that throughout this paper I restrict attention to $B < 2$, and all previous studies that I am aware of do likewise. For $B > 2$, the local dynamics of (1) can be more complex, and this is likely to result in more complex spatiotemporal behaviour, but this parameter regime is not relevant to applications.

homoclinic to different equilibria, and which meet at a point in the A - c plane that satisfies $c = O_s(\nu^{1/2})$ and $A = O_s(\nu^{1/4})$. I will show this, and will calculate the leading order coordinates of the meeting point.

In Section 2, I describe some preliminary results on the travelling wave equations (2), and discuss the form of patterns close to the Hopf bifurcation locus in the A - c plane. The solution form changes as one moves away from this locus, and two different solution structures must be considered in other parts of the A - c plane; these are discussed in Section 3 and Section 4. In Section 5 I summarise my main results and describe their numerical verification. Finally in Section 6 I discuss the ecological implications of my results, and comment on possible directions for future work.

2. Rescaling the travelling wave equations

The homogeneous equilibria of (1) are $(0, A)$ and, if $A \geq 2B$, also

$$(u_u, w_u) = \left(\frac{A - \sqrt{A^2 - 4B^2}}{2B}, \frac{2B^2}{A - \sqrt{A^2 - 4B^2}} \right) \quad (3)$$

$$\text{and } (u_s, w_s) = \left(\frac{A + \sqrt{A^2 - 4B^2}}{2B}, \frac{2B^2}{A + \sqrt{A^2 - 4B^2}} \right). \quad (4)$$

The “desert” steady state $(0, A)$ is always stable, while (u_u, w_u) is always unstable, even to homogeneous perturbations. Pattern solutions originate from (u_s, w_s) , which is stable to homogeneous perturbations when $B < 2$, and unstable to inhomogeneous perturbations for some values of A . The condition $B < 2$ holds for any realistic parameter set [18], and I assume that it holds throughout this paper. When $B > 2$, (u_s, w_s) can become unstable to homogeneous perturbations via a Hopf bifurcation, but the resulting spatially uniform limit cycles have no relevance to applications.

As shown in Fig. 1, one boundary of the A - c parameter region in which patterns occur is the locus of Hopf bifurcations of (u_s, w_s) in the travelling wave equations (2). A straightforward calculation shows that the part of this locus with $c = O_s(\nu^{1/2})$ and $A = O_s(\nu^{1/4})$ is $A^2c = B^3\nu$ to leading order as $\nu \rightarrow \infty$ (see [42] for details). Moreover, along this locus $u_s \sim A/B$ and $w_s \sim B^2/A$, with the period of the neutrally stable oscillations $\sim 2\pi c/B$, as $\nu \rightarrow \infty$. For notational convenience I define

$$\bar{A} = A/\nu^{1/4} \quad \bar{c} = c/\nu^{1/2}; \quad (5)$$

thus in the part of the A - c plane that I am considering, \bar{A} and \bar{c} are $O_s(1)$ as $\nu \rightarrow \infty$. Then, on the basis of the behaviour near Hopf bifurcation, I set

$$\begin{aligned} \tilde{U} &= (B/\bar{A})\nu^{-1/4}U & \tilde{W} &= (\bar{A}/B^2)\nu^{1/4}W \\ \tilde{z} &= (B/\bar{c})\nu^{-1/2}z. \end{aligned} \quad (6)$$

Substituting these into (2) gives

$$\nu^{-1} (B/\bar{c}^2) d^2\tilde{U}/d\tilde{z}^2 + d\tilde{U}/d\tilde{z} + \tilde{U}^2\tilde{W} - \tilde{U} = 0 \quad (7a)$$

$$\begin{aligned} (1 + \bar{c}\nu^{-1/2}) \cdot (B^3/\bar{c}\bar{A}) d\tilde{W}/d\tilde{z} \\ + \bar{A} - \nu^{-1/2}(B^2/\bar{A})\tilde{W} - \bar{A}\tilde{U}^2\tilde{W} = 0. \end{aligned} \quad (7b)$$

As $\nu \rightarrow \infty$, these equations have the leading order form

$$d\tilde{U}/d\tilde{z} = \tilde{U} - \tilde{U}^2\tilde{W} \quad (8a)$$

$$d\tilde{W}/d\tilde{z} = \sigma^2(\tilde{U}^2\tilde{W} - 1) \quad (8b)$$

where $\sigma = \bar{A}\bar{c}^{1/2}/B^{3/2}$.

Eqs. (8) also arise in the “tusk-shaped” part of the region of the A - c plane giving patterns ($\nu^{1/2} \ll c \ll 1$; see Fig. 1), and I have studied them in detail previously [42]. I now summarise the key

results of this previous work, and prove some small extensions that are required for the present study.

Standard calculations show that the unique steady state of (8), $\tilde{U} = \tilde{W} = 1$, is stable if and only if $\sigma < 1$, with a subcritical Hopf bifurcation at $\sigma = 1$. To investigate (8) in more detail, I follow [42] and rewrite (8) in terms of

$$\mu = \sigma\tilde{U} \quad \phi = \tilde{U}\tilde{W}, \quad (9)$$

giving

$$d\mu/d\tilde{z} = \mu - \mu\phi \quad (10a)$$

$$d\phi/d\tilde{z} = \mu^2\phi - \sigma\mu + \phi - \phi^2. \quad (10b)$$

There are three steady states of (10): $(\mu, \phi) = (0, 0)$, $(\sigma, 1)$ and $(0, 1)$. For all $\sigma \in (0, 1)$, $(\mu, \phi) = (0, 0)$ is an unstable node; $(\mu, \phi) = (\sigma, 1)$ is a stable focus; and $(\mu, \phi) = (0, 1)$ is non-hyperbolic, with a stable eigenvector $(0, 1)$ and an unstable centre manifold $\phi = 1 - \sigma\mu + \mu^2 + O(\mu^3)$ for $\mu > 0$, along which $\mu = -1/(\sigma\tilde{z}) + O(1/\tilde{z}^2)$ and $\phi = 1 + 1/\tilde{z} + O(1/\tilde{z}^2)$ as $\tilde{z} \rightarrow -\infty$. Therefore there is exactly one trajectory leaving the steady state $(0, 1)$. I denote this trajectory by \mathcal{T} ; it leaves $(0, 1)$ along the centre manifold $\phi = 1 - \sigma\mu + O(\mu^2)$ and enters the half-strip $0 < \phi < 1$, $\mu > 0$. Since $d\mu/d\tilde{z} > 0$ throughout this half-strip, one of three possible cases must apply.

Case 1: \mathcal{T} first exits $0 < \phi < 1$ at a point on $\phi = 0$.

Case 2: \mathcal{T} does not leave $0 < \phi < 1$. The form of the nullclines of (10) shows that this requires $\mu \rightarrow \infty$ and $\phi \rightarrow 0$ as $\tilde{z} \rightarrow \infty$ (see [42] for details).

Case 3: \mathcal{T} first exits $0 < \phi < 1$ at a point on $\phi = 1$.

I define $\sigma^* = \sup\{\sigma \mid \sigma \in (0, 1) \text{ and case 3 applies}\}$. In [42] I prove that when $\sigma = \sigma^*$, (10) has a solution that is homoclinic to $(0, 1)$. This corresponds to a homoclinic solution of (8) that is homoclinic to a point at infinity. Numerical calculations show that $\sigma^* \approx 0.9003$, and suggest strongly that the limit cycle branch starting at the Hopf bifurcation point ($\sigma = 1$) terminates at $\sigma = \sigma^*$, the homoclinic solution; however I have not been able to prove this. Note that the results in [42] show that case 2 applies for $\sigma = \sigma^*$, but they do not exclude the possibility that case 2 also occurs for isolated values of $\sigma \in (\sigma^*, 1)$. However this is not an obstacle for any of my analysis. In fact numerical solutions suggest strongly that case 1 applies for all $\sigma \in (\sigma^*, 1)$.

I denote by $\mu_{\max}(\sigma)$ the maximum value of μ on the limit cycle branch of (10) close to its homoclinic limit at $\sigma = \sigma^*$. In [42] I prove the following:

Proposition 1 ([42]). $\mu_{\max}(\sigma) \rightarrow \infty$ as $\sigma \rightarrow \sigma^{*+}$, and the maximum value of ϕ also $\rightarrow \infty$, in proportion to μ_{\max}^2 . Additionally, part of the limit cycle solution changes over a \tilde{z} length scale that is $O(\mu_{\max}^{-2})$ as $\sigma \rightarrow \sigma^{*+}$.

I have been unable to determine analytically the rate at which $\mu_{\max} \rightarrow \infty$ as $\sigma \rightarrow \sigma^{*+}$, but numerical calculations suggest strongly that the dependence is $\mu_{\max} = O_s(\log|\sigma - \sigma^*|)$ as $\sigma \rightarrow \sigma^{*+}$ [42].

For the purposes of this paper, I require the following additional result:

Proposition 2.

- (i) For $\sigma \in (\sigma^*, 1)$ with case 1 applying, denote by $(\mu_{\text{cross}}(\sigma), 0)$ the point at which the trajectory \mathcal{T} crosses the $\phi = 0$ axis. Then for σ above and sufficiently close to σ^* , case 1 applies, and $\mu_{\text{cross}} \rightarrow \infty$ as $\sigma \rightarrow \sigma^{*+}$.
- (ii) For $\sigma \in (0, \sigma^*)$, any trajectory crossing the $\mu > 0$ part of the $\phi = 0$ axis originates from the steady state $(\mu, \phi) = (0, 0)$, and satisfies $\phi/\mu \sim -\sigma\tilde{z}$ as $\tilde{z} \rightarrow -\infty$.

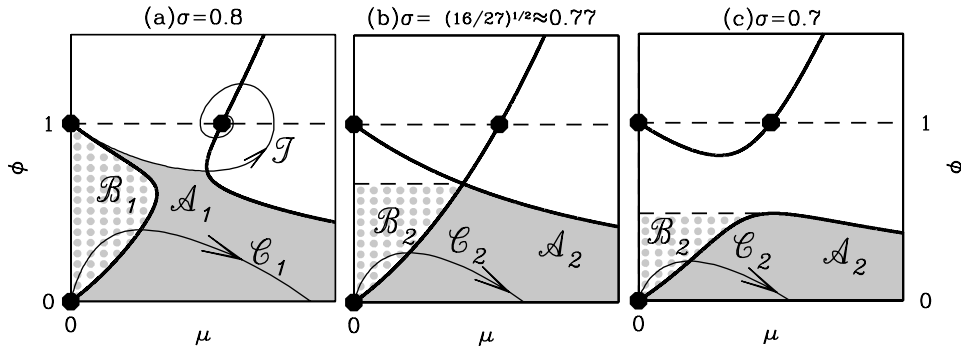


Fig. 2. An illustration of various lines and regions in the μ - ϕ plane that are referred to in the proof of Proposition 2(ii). (a) A typical case for $\sigma \in (\sqrt{16/27}, \sigma^*)$; (b) $\sigma = \sqrt{16/27}$; (c) a typical case for $\sigma \in (0, \sqrt{16/27})$. The solid shading indicates the region \mathcal{A}_1 in (a) and \mathcal{A}_2 in (b), (c). The grey dots indicate the region \mathcal{B}_1 in (a) and \mathcal{B}_2 in (b), (c). The three large black dots in each part of the figure indicate the three steady states of (10), which are $(0, 0)$, $(\sigma, 1)$ and $(0, 1)$. Thin solid lines denote solution trajectories of (10); \mathcal{C}_1 (in (a)) and \mathcal{C}_2 (in (b), (c)) are representative trajectories crossing the $\phi = 0$ axis with $\mu > 0$, and \mathcal{T} (in (a)) is the unique trajectory leaving $(1, 0)$ into the $\mu > 0$ half-plane. Thick solid lines denote the ϕ nullcline. The solution trajectories were calculated by solving (10) numerically using the routine DLSODA [43,44], which is part of the ODEPACK collection, and is freely available at www.netlib.org. The solver automatically switches between an Adams predictor–corrector method and a backward differentiation formula method.

Part (i) of this proposition was proved in [42] but part (ii) is a new result.

Proof of (ii). In [42] I showed that $\sigma^* \in (\sqrt{16/27} \approx 0.77, 1)$; in fact numerical solutions of (10) show that $\sigma^* \approx 0.9003$. The significance of $\sqrt{16/27}$ is that at this value of σ there is a qualitative change in the ϕ nullcline. Calculation of this nullcline (standard and omitted for brevity) shows that it has two branches. For $\sigma > \sqrt{16/27}$ these branches are separated by a μ interval on which there is no nullcline; for $\sigma < \sqrt{16/27}$ they are separated by a ϕ interval on which there is no nullcline; and for $\sigma = \sqrt{16/27}$ the two branches meet (Fig. 2).

I will consider separately the cases $\sqrt{16/27} < \sigma < \sigma^*$ and $\sigma \leq \sqrt{16/27}$. In the former case, I showed in [42] that the trajectory \mathcal{T} leaves $(\mu, \phi) = (0, 1)$ between the left-hand branch of the ϕ nullcline and the line $\phi = 1$, and subsequently intersects the right-hand branch of the ϕ nullcline. I denote by \mathcal{A}_1 the open part of the μ - ϕ plane between the two branches of the ϕ nullcline, the trajectory \mathcal{T} , and the line $\phi = 0$ (illustrated in Fig. 2(a)). Also, I denote by \mathcal{B}_1 the open region between $\mu = 0$ and the left-hand branch of the ϕ nullcline (Fig. 2(a)). Consider now a trajectory \mathcal{C}_1 that leaves \mathcal{A}_1 through the $\phi = 0$ axis. Throughout \mathcal{A}_1 , $d\phi/d\bar{z} < 0$ and $d\mu/d\bar{z} > 0$. Therefore \mathcal{C}_1 must enter \mathcal{A}_1 through the left hand branch of the ϕ nullcline, i.e. from \mathcal{B}_1 . (Recall that entry from $(\mu, \phi) = (0, 1)$ is not possible since \mathcal{T} is the only trajectory leaving this steady state and going into $\mu > 0$). Within \mathcal{B}_1 , $d\phi/d\bar{z} > 0$ and $d\mu/d\bar{z} > 0$. Now $\mu = 0, 0 < \phi < 1$ is a solution trajectory, and all trajectories crossing the left-hand part of the ϕ nullcline do so out of \mathcal{B}_1 . Therefore \mathcal{C}_1 must enter \mathcal{B}_1 from the steady state $\mu = \phi = 0$ (illustrated in Fig. 2(a)).

I consider now the case $\sigma \leq \sqrt{16/27}$. I denote by \mathcal{A}_2 the open region in the μ - ϕ plane between $\phi = 0$ and the lower branch of the ϕ nullcline, and by \mathcal{B}_2 the open region between $\mu = 0$, the lower branch of the ϕ nullcline, and the line $\phi = \phi_{\max}$ (illustrated in Fig. 2(b) and (c)). Here ϕ_{\max} is the ϕ coordinate of the (unique) local maximum of the lower branch of the ϕ nullcline; note that for $\sigma = \sqrt{16/27}$, this local maximum is the intersection point of the two nullcline branches. Consider now a trajectory \mathcal{C}_2 leaving \mathcal{A}_2 through $\phi = 0$. Since $d\mu/d\bar{z} > 0$ and $d\phi/d\bar{z} < 0$ throughout \mathcal{A}_2 , \mathcal{C}_2 must enter \mathcal{A}_2 from \mathcal{B}_2 ; note that all trajectories crossing the lower branch of the ϕ nullcline to the right of the local maximum do so out of \mathcal{A}_2 . But $d\mu/d\bar{z} > 0$ and $d\phi/d\bar{z} > 0$ throughout \mathcal{B}_2 , and $\mu = 0, 0 < \phi < 1$ is a solution trajectory; thus \mathcal{C}_2 must enter \mathcal{B}_2 from $\mu = \phi = 0$ (illustrated in Fig. 2(b) and (c)).

The final part of the proposition concerns the slope of the trajectories \mathcal{C}_1 and \mathcal{C}_2 at $(0, 0)$. The stability matrix of (10) at this

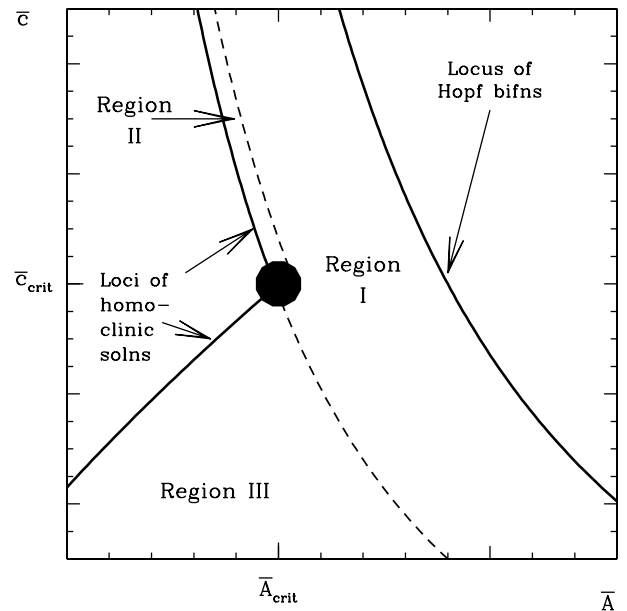


Fig. 3. A schematic illustration of the subdivision of the part of the \bar{A} - \bar{c} parameter plane in which pattern solutions exist; recall that $\bar{A} = A/v^{1/4}$ and $\bar{c} = c/v^{1/2}$. The solid lines indicate the boundaries of the region in which pattern solutions exist, and the dashed lines separate the three regions in which the patterns have different mathematical structures. The large central dot indicates the point $(\bar{A}_{\text{crit}}, \bar{c}_{\text{crit}})$, which is defined in the main text.

steady state is $\begin{bmatrix} 1 & 0 \\ -\sigma & 1 \end{bmatrix}$. Therefore it is a degenerate unstable node, and standard theory implies that $\mu = O_s(e^{\bar{z}})$ and $\phi = O_s(-\sigma \bar{z} e^{\bar{z}})$ as $\bar{z} \rightarrow -\infty$ on any trajectory originating from this steady state. This completes the proof of part (ii) of Proposition 2. \square

Proposition 1 implies that for σ sufficiently close to σ^* , (8) is not the leading order form of (7). Since the limit cycle solution changes over a length scale that is $O(\mu_{\max}^{-2})$ as $\sigma \rightarrow \sigma^{*+}$, the term $v^{-1}(B/\bar{c}^2)d^2\tilde{U}/d\bar{z}^2$ can only be neglected to leading order as $v \rightarrow \infty$ if $\mu_{\max}^2 \ll v$. Similarly since $\tilde{W} = O_s(\mu_{\max})$ as $\sigma \rightarrow \sigma^{*+}$, the term $v^{-1/2}(B^2/\bar{A})\tilde{W}$ can only be neglected if $\mu_{\max} \ll v^{1/2}$. As σ is increased towards σ^* , both of these conditions fail when $\mu_{\max} = O_s(v^{1/2})$.

I will show that the part of the A - c plane with $A = O_s(v^{1/4})$ and $c = O_s(v^{1/2})$ subdivides naturally into three regions; these are illustrated schematically in Fig. 3. In each of these regions, limit cycle solutions of (2) (i.e. patterns) have different mathematical

structures. My results thus far enable the characterisation of patterns in “region I”, which is the part of the $\bar{A}-\bar{c}$ plane to the left of the locus of Hopf bifurcations ($\bar{A}^2\bar{c} = B^3$) and in which $\mu_{\max} \ll \nu^{1/2}$. In this region, pattern solutions of (2) are limit cycle solutions of the reduced system (8), to leading order as $\nu \rightarrow \infty$. Note that the numerical evidence that $\mu_{\max} = O_s(\log(\sigma - \sigma^*))$ as $\sigma \rightarrow \sigma^{*+}$ suggests that the transition between region I and regions II and III in Fig. 3 lies exponentially close (in ν , as $\nu \rightarrow \infty$) to the curve $\bar{A}^2\bar{c} = \sigma^{*2}B^3$ (i.e. $\sigma = \sigma^*$).

The remainder of the paper considers patterns in regions II and III of the $\bar{A}-\bar{c}$ plane.

3. Pattern solutions in region II

In comparison to the patterns in region I of the $\bar{A}-\bar{c}$ plane (see Fig. 3), patterns in the other parts of the plane are significantly more complicated. They must be considered in matched layers, each of which has a different scaling with respect to ν . The patterns in region II have some similarities to those in part of the “tusk-shaped” region, which I have studied previously in [42], although there are important differences in detail; those in region III are quite different. For notational convenience, I make the substitution $\epsilon = (\bar{c}/B)\nu^{-1/2}$, so that (7) becomes

$$\epsilon^2(B^3/\bar{c}^4) d^2\tilde{U}/d\tilde{z}^2 + d\tilde{U}/d\tilde{z} + \tilde{U}^2\tilde{W} - \tilde{U} = 0 \quad (11a)$$

$$(1 + B\epsilon) d\tilde{W}/d\tilde{z} + \sigma^2(1 - \tilde{U}^2\tilde{W}) - \epsilon\tilde{W} = 0. \quad (11b)$$

(Recall that $\sigma^2 = \bar{A}^2\bar{c}/B^3$.) The region II solution consists of four layers, which I present in a clockwise order going round the limit cycle in the $\tilde{U}-\tilde{W}$ plane; this is the direction of decreasing \tilde{z} .

3.1. The solution in layer 1

There are no rescalings in this layer, so the variables are $\tilde{U} = \tilde{U}_1$, $\tilde{W} = \tilde{W}_1$, $\tilde{z} = \tilde{z}_1$, with the governing equations being (8).

3.2. The solution in layer 2

I will show in Section 3.6 that the solution of (8) required for $(\tilde{U}_1, \tilde{W}_1)$ corresponds to the trajectory \mathcal{T} of (10). Further, I will show in Section 3.7 that on the limit cycle in region II, the minimum of \tilde{U} occurs at the point of matching between “layer 2” and “layer 3”. The first of these layers reflects the slow increase of \tilde{U} from its minimum, mirroring the algebraic departure of \mathcal{T} from $(\mu, \phi) = (0, 1)$. Therefore it involves slow changes with respect to \tilde{z} , and the appropriate rescalings are

$$\tilde{U}_2 = \tilde{U}/\epsilon \quad \tilde{W}_2 = \epsilon\tilde{W} \quad \tilde{z}_2 = \epsilon\tilde{z} \quad (12)$$

$$\Rightarrow \epsilon^4(B^3/\bar{c}^4) d^2\tilde{U}_2/d\tilde{z}_2^2 + \epsilon d\tilde{U}_2/d\tilde{z}_2 + \tilde{U}_2^2\tilde{W}_2 - \tilde{U}_2 = 0$$

$$(1 + B\epsilon) d\tilde{W}_2/d\tilde{z}_2 + \sigma^2(1 - \epsilon\tilde{U}_2^2\tilde{W}_2) - \tilde{W}_2 = 0.$$

This implies that the leading order equations are

$$\tilde{U}_2(\tilde{U}_2\tilde{W}_2 - 1) = 0 \quad d\tilde{W}_2/d\tilde{z}_2 + \sigma^2 - \tilde{W}_2 = 0, \quad (13)$$

and thus to leading order,

$$\tilde{W}_2 = \sigma^2 - k_2 e^{\tilde{z}_2} \quad (14a)$$

$$\text{and either } \tilde{U}_2 = (\sigma^2 - k_2 e^{\tilde{z}_2})^{-1} \quad (14b)$$

$$\text{or } \tilde{U}_2 = 0; \quad (14c)$$

here k_2 is a constant of integration. Since \tilde{z}_1 and \tilde{z}_2 involve different scalings, it is necessary that the behaviour of $(\tilde{U}_1, \tilde{W}_1)$ as $\tilde{z}_1 \rightarrow$

$-\infty$ matches that of $(\tilde{U}_2, \tilde{W}_2)$ at a finite matching point, which I arbitrarily take as $\tilde{z}_2 = 0$. The solution (14a) for \tilde{W}_2 can easily be expanded as a power series about $\tilde{z}_2 = 0$. Using the scalings (12), it follows that the behaviour of \tilde{W}_1 as $\tilde{z}_1 \rightarrow -\infty$ must match $(\sigma^2 - k_2)/\epsilon - k_2\tilde{z}_1 + \dots$. Since \tilde{W}_1 cannot contribute an $O_s(1/\epsilon)$ term, this requires $k_2 = \sigma^2$. Then if (14b) applies, matching of \tilde{U}_1 and \tilde{U}_2 requires $\tilde{U}_1 \sim 1/(-\sigma^2\tilde{z}_1)$ as $\tilde{z}_1 \rightarrow -\infty$, while if \tilde{U}_2 is given by (14c) then the matching condition is simply $\tilde{U}_1 \rightarrow 0$ as $\tilde{z}_1 \rightarrow -\infty$. Using (9), the corresponding solution of (10) must approach $\mu = 0$ as $\tilde{z}_1 \rightarrow -\infty$. The only solution satisfying this condition is the trajectory \mathcal{T} , defined in Section 2; this holds regardless of which of (14b) and (14c) applies in layer 2.

3.3. The solution in layer 3

The limit cycle has a slow departure from the point at which \tilde{U} has its minimum, and this is reflected in the rescaling of \tilde{z} in layer 2. By contrast, the decrease of \tilde{U} to its minimum does not require a rescaling of \tilde{z} , although \tilde{U} and \tilde{W} must be rescaled as in Section 3.2:

$$\tilde{U}_3 = \tilde{U}/\epsilon \quad \tilde{W}_3 = \epsilon\tilde{W} \quad \tilde{z}_3 = \tilde{z} \Rightarrow \epsilon^2(B^3/\bar{c}^4) d^2\tilde{U}_3/d\tilde{z}_3^2 + d\tilde{U}_3/d\tilde{z}_3 + \tilde{U}_3^2\tilde{W}_3 - \tilde{U}_3 = 0 \quad (15a)$$

$$(\epsilon^{-1} + B) d\tilde{W}_3/d\tilde{z}_3 + \sigma^2(1 - \epsilon\tilde{U}_3^2\tilde{W}_3) - \tilde{W}_3 = 0. \quad (15b)$$

Intuitively, the difference in the scalings of \tilde{z} in layers 2 and 3 reflects the fact that the stable manifold of (10) at $(\mu, \phi) = (0, 1)$ is an eigenvector, while the unstable manifold involves algebraic dependence on \tilde{z} . To leading order as $\epsilon \rightarrow 0$, the solution of (15) is

$$\tilde{W}_3 = k_3 \quad (16a)$$

$$\text{and either } \tilde{U}_3 = [k_3 - h_3 \exp(-\tilde{z}_3)]^{-1} \quad (16b)$$

$$\text{or } \tilde{U}_3 = 0 \quad (16c)$$

where k_3 and h_3 are constants of integration. The condition for matching (16) to the layer 2 solution is $\lim_{\tilde{z}_2 \rightarrow -\zeta} (\tilde{U}_2, \tilde{W}_2) = \lim_{\tilde{z}_3 \rightarrow +\infty} (\tilde{U}_3, \tilde{W}_3)$ for some finite $\zeta > 0$. Therefore $k_3 = \sigma^2(1 - e^{-\zeta})$, and if (14b)/(14c) applies in layer 2 then (16b)/(16c) is the required solution for \tilde{U}_3 .

3.4. The solution in layer 4

Layers 1–3 are very similar to those in the layered solution presented in [42], which is relevant for some values of A when $\nu^{1/2} \ll c \ll 1$. The key differences between that case and the one considered here are in layer 4, which is a transition layer linking layer 3 and layer 1, and in which variation with respect to \tilde{z} is rapid. The appropriate scalings are

$$\tilde{U}_4 = \epsilon\tilde{U} \quad \tilde{W}_4 = \epsilon\tilde{W} \quad \tilde{z}_4 = \tilde{z}/\epsilon^2 \Rightarrow (B^3/\bar{c}^4) d^2\tilde{U}_4/d\tilde{z}_4^2 + d\tilde{U}_4/d\tilde{z}_4 + \tilde{U}_4^2\tilde{W}_4 - \epsilon^2\tilde{U}_4 = 0$$

$$(1 + B\epsilon) d\tilde{W}_4/d\tilde{z}_4 + \sigma^2(\epsilon^3 - \tilde{U}_4^2\tilde{W}_4) - \epsilon^3\tilde{W}_4 = 0.$$

Therefore the leading order equations are

$$(B^3/\bar{c}^4) d\tilde{U}_4/d\tilde{z}_4 + \tilde{U}_4 + \tilde{W}_4/\sigma^2 = k_4 \quad (17a)$$

$$d\tilde{W}_4/d\tilde{z}_4 - \sigma^2\tilde{U}_4^2\tilde{W}_4 = 0 \quad (17b)$$

where k_4 is a constant of integration. I require a solution of these equations whose limiting form as $\tilde{z}_4 \rightarrow +\infty$ matches the behaviour of the layer 3 solution as \tilde{z}_3 approaches an arbitrary finite matching point, which I take as $\tilde{z}_3 = 0$. This implies that $\tilde{W}_4 \rightarrow k_3$ as $\tilde{z}_4 \rightarrow +\infty$, but the corresponding condition for \tilde{U}_4 requires more careful consideration. There are three possibilities.

Possibility 1: If (16b) holds with $h_3 \neq k_3$, then $\tilde{U}_3 = 1/(k_3 - h_3) + O(\tilde{z}_3)$ as $\tilde{z}_3 \rightarrow 0$. This cannot match with \tilde{U}_4 because of the different scalings for \tilde{U} in the two layers.

Possibility 2: If (16b) holds with $h_3 = k_3$, then $\tilde{U}_3 = 1/(k_3\tilde{z}_3) + O(\tilde{z}_3^2)$ as $\tilde{z}_3 \rightarrow 0$. Then matching requires that $\tilde{U}_4 \sim 1/(k_3\tilde{z}_4)$ as $\tilde{z}_4 \rightarrow +\infty$.

Possibility 3: If (16c) holds, then matching requires that $\tilde{U}_4 = o(1/\tilde{z}_4)$ as $\tilde{z}_4 \rightarrow +\infty$.

3.5. A detailed study of Eqs. (17)

In order to proceed with the construction of the matched asymptotic solution, I require the following result concerning Eqs. (17).

Proposition 3.

- (i) For all values B, \bar{c}, σ and k_4 , there are infinitely many solutions of (17) for which $\tilde{U}_4 \rightarrow 0^+$ and $\tilde{W} \rightarrow k_4\sigma^2$ as $\tilde{z}_4 \rightarrow +\infty$. These solutions can be divided into two categories:
 - Type I: The approach to $(0, k_4\sigma^2)$ is exponential in \tilde{z}_4 . There is exactly one such solution.
 - Type II: The approach to $(0, k_4\sigma^2)$ is algebraic in \tilde{z}_4 , with $\tilde{U}_4 \sim 1/(k_4\sigma^2\tilde{z}_4)$ as $\tilde{z}_4 \rightarrow +\infty$. There is a one-parameter family of such solutions.
- (ii) There is a number $\delta^* \in (0, 4/\sqrt{3} \approx 2.31)$ such that the behaviour of these solutions as $\tilde{z}_4 \rightarrow -\infty$ is as follows.
 - If $\sigma k_4 B^{3/2} < \delta^{*2}\bar{c}^2$: The type I solution $\rightarrow (+\infty, 0)$. Exactly one of the type II solutions $\rightarrow (k_4, 0)$; the remainder $\rightarrow (\pm\infty, 0)$.
 - If $\sigma k_4 B^{3/2} = \delta^{*2}\bar{c}^2$: The type I solution $\rightarrow (k_4, 0)$, and the type II solutions $\rightarrow (-\infty, 0)$.
 - If $\sigma k_4 B^{3/2} > \delta^{*2}\bar{c}^2$: The type I solution and all of the type II solutions $\rightarrow (-\infty, 0)$.

Numerical solutions of (17) show that $\delta^* \approx 1.16$.

Proof. Rescaling and proof of (i). I begin by rescaling (17) via the substitutions

$$\tilde{U}_4 = k_4 P \quad \tilde{W}_4 = \sigma^2 k_4 Q \quad \tilde{z}_4 = Z/(\sigma^2 k_4^2)$$

$$\delta = \sigma k_4 B^{3/2} / \bar{c}^2$$

giving the equations

$$dP/dZ = (1 - P - Q)/\delta^2 \tag{18a}$$

$$dQ/dZ = P^2 Q. \tag{18b}$$

The steady state $(0, 1)$ of (18) is non-hyperbolic. Standard calculations show that it has a stable eigenvector $(1, 0)$ and a stable centre manifold on which $P = 1/Z + O(1/Z^2)$, $Q = 1 - 1/Z + O(1/Z^2)$ as $Z \rightarrow +\infty$. Part (i) of the proposition follows immediately from these results.

Definition of the function \mathcal{F} . I denote by $\Gamma(\delta)$ the (unique) trajectory of (18) that approaches $(0, 1)$ along the stable eigenvector from the $P > 0$ half-plane. Since $dQ/dZ > 0$ throughout the first quadrant, this trajectory approaches $(0, 1)$ from within the open triangular region \mathcal{R}_1 , illustrated in Fig. 4 and defined by $P < 1, Q < 1, P + Q > 1$.

Since $dQ/dZ > 0$ on the part of the boundary of \mathcal{R}_1 formed by $P + Q = 1$, with $dP/dZ < 0$ on the part of the boundary formed by $P = 1$, any trajectory leaving \mathcal{R}_1 must do so through $Q = 1$. Noting that $dQ/dZ > 0$ whenever $Q > 0$, it follows that $\Gamma(\delta)$ must enter \mathcal{R}_1 exactly once. I define

$$\mathcal{F}(\delta) = \begin{cases} Q^* & \text{if } \Gamma(\delta) \text{ enters } \mathcal{R}_1 \text{ at } (1, Q^*) \\ -Q^* & \text{if } \Gamma(\delta) \text{ enters } \mathcal{R}_1 \text{ at } (1 - Q^*, Q^*). \end{cases}$$

Now $\mathcal{F}(\cdot)$ is a continuous function, because of the continuous dependence of solution trajectories on δ . Moreover away from $P + Q = 1$, $dQ/dP \rightarrow 0$ as $\delta \rightarrow 0^+$, and thus $\mathcal{F}(\delta) \rightarrow 1$ as $\delta \rightarrow 0^+$.

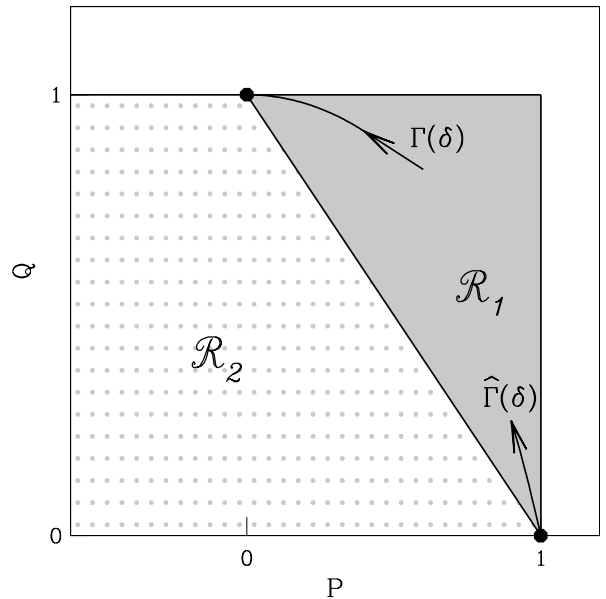


Fig. 4. An illustration of the regions \mathcal{R}_1 (solid grey shading) and \mathcal{R}_2 (grey dots) in the P - Q plane; these regions are referred to in the proof of Proposition 3. The black dots indicate the steady states $(1, 0)$ and $(0, 1)$ of Eqs. (18). Part of the trajectory $\Gamma(\delta)$ near $(0, 1)$ and part of the trajectory $\hat{\Gamma}(\delta)$ near $(1, 0)$ are also shown.

I will show that $\mathcal{F}(4/\sqrt{3}) < 0$ and that $\mathcal{F}(\cdot)$ is a decreasing function. Together these imply that there is exactly one value of $\delta \in (0, 4/\sqrt{3})$, which I denote by δ^* , satisfying $\mathcal{F}(\delta^*) = 0$, i.e. for which $\mathcal{T}(\delta^*)$ enters \mathcal{R}_1 from the steady state $(1, 0)$.

Proof that $\mathcal{F}(4/\sqrt{3}) < 0$. Since dP/dZ has constant sign in \mathcal{R}_1 , it is appropriate to use P to parametrise the part of $\Gamma(\delta)$ in \mathcal{R}_1 . On this part of $\Gamma(\delta)$ I define $\rho(P) = (1 - Q(P))/P$. Then (18) implies that

$$d\rho/dP = \frac{\delta^2(1 - P\rho)}{1 - \rho} - \rho/P$$

$$> \delta^2(1 - P) - \rho/P \quad \text{since } 0 < P, \rho < 1 \text{ in } \mathcal{R}_1$$

$$\Rightarrow d(P\rho)/dP > \delta^2(P - P^2)$$

$$\Rightarrow \rho > \delta^2 \left(\frac{1}{2}P - \frac{1}{3}P^2 \right) \quad \text{since } \lim_{P \rightarrow 0^+} \rho = 0.$$

This inequality holds for all values of P such that $\Gamma(\delta)$ is in \mathcal{R}_1 . But $\rho < 1$ throughout \mathcal{R}_1 , with $\rho = 1$ corresponding to the boundary $P + Q = 1$ of \mathcal{R}_1 . Now $\delta^2(\frac{1}{2}P - \frac{1}{3}P^2) = 1$ when $\delta = 4/\sqrt{3}$ and $P = 3/4$. Therefore when $\delta = 4/\sqrt{3}$, $\mathcal{T}(\delta)$ must enter \mathcal{R}_1 through $P + Q = 1$ at a value of $P \in (0, 3/4)$, implying that $\mathcal{F}(4/\sqrt{3}) < 0$.

Proof that $\mathcal{F}(\cdot)$ is decreasing. Suppose that $\mathcal{F}(\delta_2) > \mathcal{F}(\delta_1)$ for some $\delta_2 > \delta_1$. Recall that by definition $\Gamma(\delta)$ approaches $(0, 1)$ along the eigenvector $(1, 0)$. Power series expansion shows that $\Gamma(\delta)$ has the form $Q = 1 - \frac{1}{2}\delta^2 P^2 + O(P^3)$ as $P \rightarrow 0$, implying that sufficiently close to $(0, 1)$, $\Gamma(\delta_1)$ lies above $\Gamma(\delta_2)$ in the P - Q plane. But since $\mathcal{F}(\delta_2) > \mathcal{F}(\delta_1)$, $\Gamma(\delta_1)$ and $\Gamma(\delta_2)$ must intersect at one or more points in \mathcal{R}_1 . Let $(P_{\text{int}}, Q_{\text{int}})$ be the intersection point with the largest value of $Q < 1$. Then $(0, 1)$ and $(P_{\text{int}}, Q_{\text{int}})$ are both on $\Gamma(\delta_1)$ and also on $\Gamma(\delta_2)$, with $\Gamma(\delta_1)$ lying above $\Gamma(\delta_2)$ for $0 < P < P_{\text{int}}$. It follows that

$$\frac{dQ}{dP}(P_{\text{int}}, Q_{\text{int}}; \Gamma(\delta_1)) \leq \frac{dQ}{dP}(P_{\text{int}}, Q_{\text{int}}; \Gamma(\delta_2)) < 0.$$

But dividing (18b) by (18a) reveals that dQ/dP is a (negative) strictly decreasing function of δ throughout \mathcal{R}_1 , which is a contradiction.

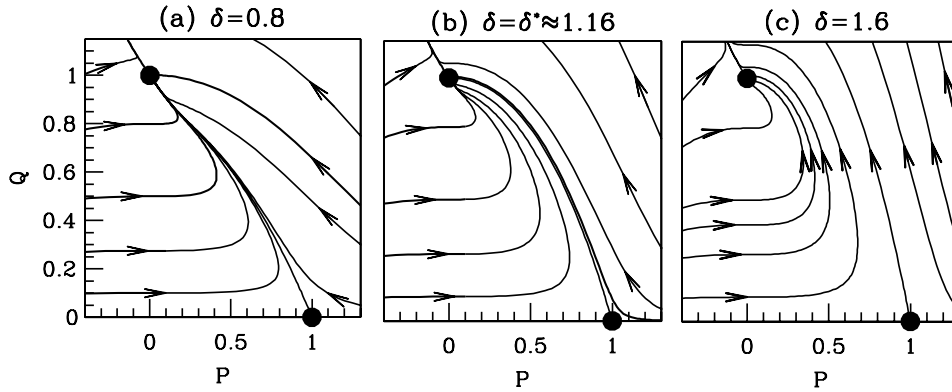


Fig. 5. Typical examples of phase portraits of Eqs. (18) for (a) $\delta < \delta^*$; (b) $\delta = \delta^*$; (c) $\delta > \delta^*$. The large dots indicate the steady states $(1, 0)$ and $(0, 1)$. The equations were solved numerically using the routine `DLSDA` [43,44], which is part of the `ODEPACK` collection, and is freely available at www.netlib.org. The solver automatically switches between an Adams predictor–corrector method and a backward differentiation formula method.

The region \mathcal{R}_2 . I define \mathcal{R}_2 as the region $0 < Q < 1, P + Q < 1$ (illustrated in Fig. 4). Now $dQ/dZ \geq 0$ on the part of the boundary of \mathcal{R}_2 formed by $Q = 1$, while $dQ/dZ = 0$ on $Q = 0$. Also $dP/dZ > 0$ throughout \mathcal{R}_2 . Therefore all trajectories in \mathcal{R}_2 must originate from $P = -\infty$, and (18) implies that the corresponding limiting value of Q must be 0.

Completion of the proof. A few further details of the P – Q phase plane are needed to complete the proof. Apart from $\Gamma(\delta)$ (which is the type I solution), all trajectories approaching $(1, 0)$ from $P > 0$ (the type II solutions) do so along the stable centre manifold, and therefore lie below $\mathcal{T}(\delta)$ in the phase plane. Turning to the steady state $(1, 0)$, this is a saddle point. Therefore exactly one trajectory leaves $(1, 0)$ and goes into the $Q > 0$ half-plane; I denote this trajectory by $\widehat{\Gamma}(\delta)$. Standard calculation of the corresponding eigen-vector shows that $\widehat{\Gamma}(\delta)$ leaves $(1, 0)$ and goes into \mathcal{R}_1 .

I now consider in turn the three cases in the statement of part (ii) of the proposition; the corresponding phase planes are illustrated schematically in Fig. 5.

If $\sigma k_4 B^{3/2} < \delta^* \bar{c}^2$, then $\mathcal{F}(\delta) > 0$, implying that Γ (the type I solution) originates from $(+\infty, 0)$. I denote by $\widehat{\mathcal{R}}_1$ the part of \mathcal{R}_1 lying below Γ . Then $\widehat{\Gamma}$ enters $\widehat{\mathcal{R}}_1$, and the only possible exit point is $(0, 1)$, which $\widehat{\Gamma}$ must approach along the stable centre manifold. Type II trajectories lying below $\widehat{\Gamma}$ must enter $\widehat{\mathcal{R}}_1$ from \mathcal{R}_2 , and thus must originate from $(-\infty, 0)$, while those lying between $\widehat{\Gamma}$ and Γ must enter $\widehat{\mathcal{R}}_1$ through $P = 1$, and must therefore originate from $(+\infty, 0)$.

If $\sigma k_4 B^{3/2} = \delta^* \bar{c}^2$, then $\mathcal{F}(\delta) = 0$, implying that Γ and $\widehat{\Gamma}$ coincide. The type II trajectories must all enter \mathcal{R}_1 from \mathcal{R}_2 , and thus must originate from $(-\infty, 0)$.

If $\sigma k_4 B^{3/2} > \delta^* \bar{c}^2$, then $\mathcal{F}(\delta) < 0$. Thus type II trajectories approach $(0, 1)$ either from \mathcal{R}_2 or from the region enclosed by Γ and $P + Q = 1$. Hence the type I trajectory and all of the type II trajectories enter \mathcal{R}_1 from \mathcal{R}_2 , and thus originate from $(-\infty, 0)$.

This completes the proof of Proposition 3. \square

3.6. The conclusion of the matching process

Armed with Proposition 3, I can proceed with the matching process. I have shown in Section 3.3 that matching between layers 3 and 4 requires $(\widetilde{U}_4, \widetilde{W}_4) \rightarrow (0, k_3)$ as $\bar{z}_4 \rightarrow +\infty$. Since the only steady state of (17) with $\widetilde{U}_4 = 0$ is $(0, k_4 \sigma^2)$, this requires $k_3 = k_4 \sigma^2$. Further, if (16b) applies for \widetilde{U}_3 , then the requirement of an algebraic approach of $(\widetilde{U}_4, \widetilde{W}_4)$ to $(0, k_3)$ determines the

layer 4 solution to be of type II, while if (16c) applies, the condition $\widetilde{U}_4 = o(1/\bar{z}_4)$ as $\bar{z}_4 \rightarrow +\infty$ implies that the layer 4 solution must be of type I.

I now turn to the final stage: matching the layer 4 solution as $\bar{z} \rightarrow -\infty$ with the layer 1 solution as \bar{z}_1 approaches an (arbitrary) finite matching value, which I take to be $\bar{z}_1 = 0$. This is not possible if $\widetilde{U}_4 \rightarrow \pm\infty$ as $\bar{z}_4 \rightarrow -\infty$ because of the different scalings of \widetilde{U} and \bar{z} in the two layers. Proposition 3(ii) then implies that the layer 4 solution corresponds to the trajectory $\widehat{\Gamma}$ of (18), with $\sigma k_4 B^{3/2} \leq \delta^* \bar{c}^2$; the layer 4 solution is of type I if equality holds and type II otherwise. But from Proposition 3(i), type I solutions have an exponential approach to $(0, k_4 \sigma^2)$, which is inconsistent with possibility 2 in Section 3.4. Therefore possibility 3 must apply, i.e. (16c) is the relevant solution in layer 3 if $\sigma k_4 B^{3/2} = \delta^* \bar{c}^2$. Similarly (16b) is the relevant solution if $\sigma k_4 B^{3/2} < \delta^* \bar{c}^2$. In both cases, the leading order solutions for $(\widetilde{U}_4, \widetilde{W}_4) \rightarrow (k_4, 0)$ as $\bar{z}_4 \rightarrow -\infty$. A matched solution of the type considered in this section is not possible if $\sigma k_4 B^{3/2} > \delta^* \bar{c}^2$.

For U , the matching condition is therefore $\widetilde{U}_1(0) = k_4/\epsilon$. For \widetilde{W} , the matching condition cannot be determined from leading order terms alone, because terms of order ϵ and ϵ^2 in the asymptotic expansion of W_4 would contribute. However, a detailed investigation (omitted for brevity) shows that the first term in this expansion with a non-zero limit as $\bar{z}_4 \rightarrow -\infty$ is $O_s(\epsilon^3)$. Therefore, I require $W_1(0) = 0$ to leading order.

I have shown that the solution for $(\widetilde{U}_1, \widetilde{W}_1)$ corresponds to the unique trajectory \mathcal{T} of (10) leaving $(\mu, \phi) = (0, 1)$ and going into the first quadrant. Therefore case 1 of Section 2 must hold, and the matching condition is $\widetilde{U}_{1,\text{cross}} = k_4/\epsilon$; recall that $\widetilde{U}_{1,\text{cross}}$ is defined in the statement of Proposition 2(i). This is possible because $\widetilde{U}_{1,\text{cross}} \rightarrow \infty$ as $\sigma \rightarrow \sigma^{*+}$. I have been unable to determine analytically the rate at which $\widetilde{U}_{1,\text{cross}} \rightarrow \infty$ as $\sigma \rightarrow \sigma^{*+}$, but numerical calculations suggest that $\widetilde{U}_{1,\text{cross}}(\sigma) = O_s(\log(\sigma - \sigma^*))$ [42]. This would imply that σ is exponentially close (in ϵ) to σ^* as $\epsilon \rightarrow 0$.

Formally, this concludes the matching process, with all constants of integration determined as follows.

- Matching result 1: $k_2 = \sigma^2, k_3 = \sigma^2(1 - e^{-\zeta}), k_4 = 1 - e^{-\zeta}$.
- Matching result 2: (14c) and (16c) apply in layers 2 and 3 respectively if $B^{3/2}\sigma(1 - e^{-\zeta}) = \delta^* \bar{c}^2$.
(14b) and (16b) apply in layers 2 and 3 respectively if $B^{3/2}\sigma(1 - e^{-\zeta}) > \delta^* \bar{c}^2$.
There is no matched solution if $B^{3/2}\sigma(1 - e^{-\zeta}) < \delta^* \bar{c}^2$.
- Matching result 3: $(1 - e^{-\zeta}) = \epsilon \widetilde{U}_{1,\text{cross}}(\sigma)$.

These conditions determine k_2, k_3, k_4 and ζ as functions of \bar{A}, \bar{c}, B and ν ; note that together, these four parameters specify σ and ϵ .

3.7. The implication of the matched solution

Matching result 3 in Section 3.6 requires that $\tilde{U}_{1,\text{cross}}(\sigma) \gg 1$ as $\epsilon \rightarrow 0$, implying that the solution constructed in Sections 3.1–3.6 is only valid in a strip of the \bar{A} – \bar{c} plane close to $\bar{A}^2\bar{c} = \sigma^{*2}B^3$ (i.e. $\sigma = \sigma^*$), whose width $\rightarrow 0$ as $\epsilon \rightarrow 0$. My numerical results on the rate at which $\tilde{U}_{1,\text{cross}} \rightarrow \infty$ as $\sigma \rightarrow \sigma^{*+}$ suggest that the width is actually exponentially small in ϵ as $\epsilon \rightarrow 0$, but I have been unable to prove this. Away from $\sigma = \sigma^*$ (in region I in Fig. 3) it is the limit cycle solution of (8) that is relevant for pattern solutions of (1). In the thin strip, the period of the limit cycles is dominated by layer 2 (“thick”), and is ζ/ϵ to leading order. Therefore, as expected, the layer structure breaks down as $\zeta \rightarrow 0^+$, corresponding to the solution approaching a limit cycle solution of (8). As $\zeta \rightarrow +\infty$, the period of the limit cycle $\rightarrow \infty$, so the limit cycle approaches a homoclinic solution. This solution is homoclinic to the limiting location of the point corresponding to $\bar{z}_2 = -\zeta$, as $\zeta \rightarrow \infty$. This is the point of matching between layers 2 and 3, which is

$$(\tilde{U}, \tilde{W}) = \begin{cases} \left(\frac{\epsilon}{\sigma^2(1-e^{-\zeta})}, \frac{\sigma^2(1-e^{-\zeta})}{\epsilon} \right) \\ \text{if } B^{3/2}\sigma(1-e^{-\zeta}) < \delta^*\bar{c}^2 \\ \left(0, \frac{\sigma^2(1-e^{-\zeta})}{\epsilon} \right) \\ \text{if } B^{3/2}\sigma(1-e^{-\zeta}) = \delta^*\bar{c}^2. \end{cases}$$

Taking the limit as $\zeta \rightarrow \infty$, this shows that the homoclinic solution is homoclinic to the point

$$(\epsilon/\sigma^2, \sigma^2/\epsilon) = \left(\frac{\epsilon B^3}{\bar{A}^2\bar{c}}, \frac{\bar{A}^2\bar{c}}{\epsilon B^3} \right) = \left(\frac{B^2}{\bar{A}^2\nu^{1/2}}, \frac{\bar{A}^2\nu^{1/2}}{B^2} \right)$$

$$\text{if } B^{3/2}\sigma < \delta^*\bar{c}^2$$

$$\text{and } (0, \sigma^2/\epsilon) = \left(0, \frac{\bar{A}^2\bar{c}}{\epsilon B^3} \right) = \left(0, \frac{\bar{A}^2\nu^{1/2}}{B^2} \right)$$

$$\text{if } B^{3/2}\sigma = \delta^*\bar{c}^2.$$

Recall that provided $A \geq 2B$, the model equations (1) have three homogeneous steady states:

$$(u, w) = (0, A) \sim (0, \bar{A}\nu^{1/4}) \quad \text{as } \nu \rightarrow \infty,$$

$$\text{which corresponds to } (\tilde{U}, \tilde{W}) = \left(0, \frac{\bar{A}^2\nu^{1/2}}{B^2} \right)$$

$$(u, w) = (u_u, w_u) \sim (B\nu^{-1/4}/\bar{A}, \bar{A}\nu^{1/4}) \quad \text{as } \nu \rightarrow \infty,$$

$$\text{which corresponds to } (\tilde{U}, \tilde{W}) = \left(\frac{B^2}{\bar{A}^2\nu^{1/2}}, \frac{\bar{A}^2\nu^{1/2}}{B^2} \right)$$

$$(u, w) = (u_s, w_s) \sim (\bar{A}\nu^{1/4}/B, B^2\nu^{-1/4}/\bar{A}) \quad \text{as } \nu \rightarrow \infty,$$

$$\text{which corresponds to } (\tilde{U}, \tilde{W}) = (1, 1).$$

Therefore in terms of the original model variables, I have shown that the homoclinic solution is homoclinic to (u_u, w_u) if $\bar{A} < \delta^*\bar{c}^{3/2}$ and to $(0, A)$ if $\bar{A} = \delta^*\bar{c}^{3/2}$.

Moreover, the homoclinic solution occurs when $\sigma = \sigma^* + o(1)$; recall that $\sigma = \bar{A}\bar{c}^{1/2}/B^{3/2}$. Therefore I am able to conclude that to leading order as $\nu \rightarrow \infty$, there is a locus of homoclinic solutions consisting of the part of the curve $\bar{A}^2\bar{c} = B^3\sigma^{*2}$ (i.e. $\sigma = \sigma^*$) with $\bar{c} \geq \bar{c}_{\text{crit}} = (\sigma^*/\delta^*)^{1/2}B^{3/4}$, i.e. $\bar{A} \leq \bar{A}_{\text{crit}} = \sigma^{*3/4}\delta^{*1/4}B^{9/8}$. Again to leading order as $\nu \rightarrow \infty$, the solutions are homoclinic to $(0, A)$ at $\bar{c} = \bar{c}_{\text{crit}}$, and to (u_u, w_u) when $\bar{c} > \bar{c}_{\text{crit}}$.

4. Pattern solutions in region III

Region III of the \bar{A} – \bar{c} plane (see Fig. 3) is defined by $\sigma = \bar{A}\bar{c}^{1/2}/B^{3/2} < \sigma^*$ and $\bar{c} < \bar{c}_{\text{crit}}$. Recall that for the leading order pattern equations (8), there are no limit cycle solutions when $\sigma < \sigma^*$. Moreover, the matched solution constructed in Section 3 is only valid when $\bar{c} \geq \bar{c}_{\text{crit}}$. Therefore a new solution structure must apply in region III. It consists of three matched layers, which correspond directly to layers 1, 2 and 4 in Section 3, and which I will denote by 1A, 2A and 4A. Note that when $\bar{c} = \bar{c}_{\text{crit}}$, layer 3 plays no role at all to leading order, since the solutions for \tilde{U}_3 and \tilde{W}_3 are just constants, and for $\bar{c} < \bar{c}_{\text{crit}}$ there is no equivalent of this layer in the solution structure.

4.1. The solution in layer 1A

The rescalings (none) and leading order equations in this layer are exactly the same as in layer 1. I denote the solution by $\tilde{U}_{1A}(\bar{z}_{1A})$ and $\tilde{W}_{1A}(\bar{z}_{1A})$.

4.2. The solution in layer 2A

This corresponds to layer 2 in Section 3: it is a “thick” layer, reflecting slow changes with respect to \bar{z} . Recall that the leading order solution for \tilde{U}_2 is non-zero when $\bar{c} > \bar{c}_{\text{crit}}$, but changes to zero at $\bar{c} = \bar{c}_{\text{crit}}$. In fact, $\tilde{U}_2 = 0$ to all algebraic orders in ϵ when $\bar{c} = \bar{c}_{\text{crit}}$, and this is also the case in layer 2A, for which the appropriate rescalings are

$$\tilde{U}_{2A} \equiv 0 \quad \tilde{W}_{2A} = \epsilon\tilde{W} \quad \bar{z}_{2A} = \epsilon\bar{z}. \quad (19)$$

Substituting (19) into (11) gives, to leading order as $\epsilon \rightarrow 0$,

$$d\tilde{W}_{2A}/d\bar{z}_{2A} + \sigma^2 - \tilde{W}_{2A} = 0 \Rightarrow \tilde{W}_{2A} = \sigma^2 - k_{2A}e^{\bar{z}_{2A}} \quad (20)$$

where k_{2A} is a constant of integration. I require that the behaviour of $(\tilde{U}_{1A}, \tilde{W}_{1A})$ as $\bar{z}_{1A} \rightarrow -\infty$ matches that of $(\tilde{U}_{2A}, \tilde{W}_{2A})$ at some finite value of \bar{z}_{2A} which I arbitrarily take to be zero. Therefore I require that there is matching between $(\tilde{U}_{1A}, \tilde{W}_{1A})$ and $(0, (\sigma^2 - k_{2A})/\epsilon - k_{2A}\bar{z}_{1A} - \frac{1}{2}\epsilon k_{2A}\bar{z}_{1A}^2 + \dots)$ as $\bar{z}_{1A} \rightarrow -\infty$. Since \tilde{W}_{1A} cannot contribute an $O_s(1/\epsilon)$ term, this requires $k_{2A} = \sigma^2$ and $(\tilde{U}_{1A}, \tilde{W}_{1A}) \rightarrow (0, \infty)$ as $\bar{z}_{1A} \rightarrow -\infty$, with \tilde{U}_{1A} approaching zero at a rate that is beyond all algebraic orders, and with $\tilde{W}_{1A} \sim -\sigma^2\bar{z}_{1A}$. Using (9), this corresponds to $(\mu, \phi) \rightarrow (0, 0)$ as $\bar{z}_{1A} \rightarrow -\infty$ in (10), with $\phi/\mu \sim -\sigma\bar{z}_{1A}$. From Proposition 2(ii) it follows that the layer 1A solution corresponds to one of the solutions of (10) originating from $\phi = \mu = 0$.

4.3. The solution in layer 4A

This corresponds to layer 4 in Section 3, with the same rescalings and leading order solution for \tilde{U}_{4A} and \tilde{W}_{4A} as for \tilde{U}_4 and \tilde{W}_4 ; I denote by k_{4A} the constant of integration corresponding to k_4 . For matching to layer 2A, I require that the behaviour of $(\tilde{U}_{4A}, \tilde{W}_{4A})$ as $\bar{z}_{4A} \rightarrow \infty$ matches the layer 2A solution at a finite matching point, which I denote by $\bar{z}_{2A} = -\zeta$ (here $\zeta > 0$). Then matching requires that $\tilde{U}_{4A} \rightarrow 0$ and $\tilde{W}_{4A} \rightarrow \sigma^2 - k_{2A}e^{-\zeta}$ as $\bar{z}_{4A} \rightarrow \infty$. Moreover, since $\tilde{U}_{2A} = 0$ to all algebraic orders in ϵ , the approach of \tilde{U}_{4A} to zero as $\bar{z}_{4A} \rightarrow \infty$ must be exponential not algebraic in \bar{z}_{4A} . From Proposition 3(i) it follows that $k_{4A}\sigma^2 = \sigma^2 - k_{2A}e^{-\zeta}$, with the solution for $(\tilde{U}_{4A}, \tilde{W}_{4A})$ being of type I, defined in the statement of Proposition 3.

Turning to matching between layers 4A and 1A, this requires that the behaviour of $(\tilde{U}_{4A}, \tilde{W}_{4A})$ as $\bar{z}_{4A} \rightarrow -\infty$ matches the layer

1A solution at an arbitrary finite matching point, which I take as $\tilde{z}_{1A} = 0$. For \tilde{U} , this implies that $\tilde{U}_{1A}(0) = k_{4A}/\epsilon$. Also, since the layer 4A solution is of type I, it follows from Proposition 3(ii) that $\sigma k_{4A} B^{3/2} = \delta^* \bar{c}^2$. For \tilde{W} , the matching condition cannot be determined from leading order terms along, because terms of order ϵ and ϵ^2 in the asymptotic expansion of \tilde{W}_{4A} would contribute. However, as was the case for \tilde{W}_4 in Section 3.4, a detailed investigation (omitted for brevity) shows that the first term in this expansion with a non-zero limit as $\tilde{z}_{4A} \rightarrow -\infty$ is $O_s(\epsilon^3)$. Therefore, I require $\tilde{W}_{1A}(0) = 0$ to leading order.

The condition $(\tilde{U}_{1A}, \tilde{W}_{1A}) \sim (k_{4A}/\epsilon, 0)$ as $\epsilon \rightarrow 0$ corresponds to $(\mu, \phi) \sim (\sigma k_{4A}/\epsilon, 0)$ in (10). Hence to leading order as $\epsilon \rightarrow 0$, the layer 4 solution must correspond to the trajectory in the phase plane of (10) that crosses the $\phi = 0$ axis at the point $\mu = \sigma k_{4A}/\epsilon$. This uniquely specifies the solution. Moreover, Proposition 2(ii) shows that this trajectory also satisfies the requirement established in Section 4.2 that the layer 1A solution corresponds to a trajectory of (10) originating at $\mu = \phi = 0$, with $\phi/\mu \sim -\sigma \tilde{z}_{1A}$ as $\tilde{z}_{1A} \rightarrow -\infty$.

4.4. The conclusion of the matching process, and its implications

Taken together, the results in Sections 4.1–4.3 determine all constants of integration as follows:

- Matching result 1A: $k_{2A} = \sigma^2 = \bar{A}^2 \bar{c}/B^3$ and $k_{4A} = 1 - e^{-\zeta}$.
 Matching result 2A: the layer 1A solution corresponds to the (μ, ϕ) trajectory passing through the point $(\sigma(1 - e^{-\zeta})/\epsilon, 0)$
 Matching result 3A: $\sigma(1 - e^{-\zeta})B^{3/2} = \delta^* \bar{c}^2$
 $\Rightarrow \zeta = -\log(1 - \delta^* \bar{c}^{3/2}/\bar{A})$.

The period of the limit cycle formed by the three matched solutions is dominated by layer 2A (“thick”). Undoing the rescalings (6) and (19) shows that the pattern wavelength is therefore given by

$$(\bar{c}v^{1/2}/B) \cdot (\zeta/\epsilon) = -v \log(1 - \delta^* \bar{c}^{3/2}/\bar{A})$$

to leading order as $v \rightarrow \infty$. Note in particular that the solution is only valid when $\bar{c}^{3/2} \delta^* < \bar{A}$, with an infinite period in the limiting case $\bar{c}^{3/2} \delta^* = \bar{A}$. This is a second locus of homoclinic solutions. The locus applies only for $\bar{c} < \bar{c}_{\text{crit}}$, and the solutions are homoclinic to the point of matching between layers 2A and 4A, i.e. $(\tilde{U}, \tilde{W}) = (0, \sigma^2/\epsilon)$, which corresponds to $(U, W) = (0, A)$.

5. A summary of results and the numerical verification

The Klausmeier model (1) for banded vegetation in semi-arid environments has pattern solutions for a wide range of values of the parameters A and c , which correspond to mean annual rainfall and migration speed respectively. This paper is part of a larger study of the existence and form of pattern solutions in the ecologically relevant case of large values of the slope parameter v . In this paper I have focused on the very specific case of $A = O_s(v^{1/4})$ and $c = O_s(v^{1/2})$; from a mathematical point of view this is the most interesting and most complicated part of the A – c parameter plane. My key results are as follows; they are valid to leading order for large values of v .

1. The part of the A – c parameter plane in which patterns exist is bounded by three curves: the locus of Hopf bifurcations of (2), $A^2 c = B^3 v$, and two loci of homoclinic solutions of (2), $A^2 c = B^3 \sigma^* v$ with $c \geq (\sigma^*/\delta^*)^{1/2} B^{3/4} v^{1/2}$ and $A c^{-3/2} = \delta^* v^{-1/2}$ with $c \leq (\sigma^*/\delta^*)^{1/2} B^{3/4} v^{1/2}$. Here σ^* and δ^* are defined in Section 2 and Section 3 respectively, and numerical calculations show that $\sigma^* \approx 0.9003$ and $\delta^* \approx 1.16$.
2. The homoclinic solutions are homoclinic to (u_u, w_u) for $c > (\sigma^*/\delta^*)^{1/2} B^{3/4} v^{1/2}$ and to $(0, A)$ for $c \leq (\sigma^*/\delta^*)^{1/2} B^{3/4} v^{1/2}$. Here (u_u, w_u) is defined in (3).

3. The part of the A – c parameter plane in which patterns exist divides into three regions (see Fig. 3) in which the patterns have different solution structures.

Region I is defined by $\sigma^{*2} < A^2 c/(B^3 v) < 1$. Here the patterns correspond to limit cycle solutions of (8).

Region II is a strip of width $o(1)$ as $v \rightarrow \infty$, adjacent to the curve $A^2 c = B^3 \sigma^{*2} v$ with $c > (\sigma^*/\delta^*)^{1/2} B^{3/4} v^{1/2}$. Here the patterns consist of four matched layers, as described in Section 3.

Region III is defined by $A c^{-3/2} > \delta^* v^{1/2}$ and $c < (\sigma^*/\delta^*)^{1/2} B^{3/4} v^{-1/2}$. Here the patterns consist of three matched layers, as described in Section 4.

For numerical verification of these results, my main focus is the transition between a homoclinic solution of (2) that is homoclinic to $(U, W) = (u_u, w_u)$ and one that is homoclinic to $(U, W) = (0, A)$. Since $w_u \sim A$ as $v \rightarrow \infty$, it is most convenient to focus on the transition in U . Moreover numerical testing is facilitated by noting that in my leading order homoclinic solutions, the minimum value of U is simply u_u and 0 in the two cases. I have not attempted numerical calculation of the loci of actual homoclinic solutions of (2); rather, I approximate these via the loci of solutions of large, fixed period. I will present results on this for the specific case of $B = 0.45$ and $v = 10^4$; this case is chosen arbitrarily but it is typical. Fig. 6(a) shows the period as a function of the rainfall parameter A , for the wave speed c fixed at 61, which is significantly above the predicted threshold of $(\sigma^*/\delta^*)^{1/2} B^{3/4} v^{1/2} = 48.39$.

The period increases as A is decreased, with the homoclinic solution (period = ∞) occurring at $A = 3.96$. Fig. 6(b) shows variation in $\min(U)$ along this curve. I plot $\min(U) \cdot A/B$; since $u_u \sim B/A$ as $v \rightarrow \infty$, my analysis predicts that this expression is equal to $1 + o(1)$ as $v \rightarrow \infty$ on the homoclinic solution (i.e. in the limit as the period $\rightarrow \infty$), and this is confirmed in Fig. 6(b).

The results in Fig. 6(b) also show that a period greater than about $10^{4.8}$ is necessary to effectively approximate the homoclinic locus. Accordingly, Fig. 6(c) shows the variation in $\min(U) \cdot A/B$ remains constant at 1 as c decreases, until a sharp transition to zero occurs at $c \approx 48.5$; this is exactly as predicted by my calculations. However a fixed period of 10^4 is too low to give this behaviour: the transition to $\min(U) = 0$ occurs significantly below 48.39, and above it, $\min(U) \cdot A/B$ is significantly above 1, and is not constant.

For the parameter values $v = 10^4$ and $B = 0.45$ used in Fig. 6, the transition between $\min(U) = B/A$ and $\min(U) = 0$ on the locus of fixed period 10^5 occurs very close to, but slightly above, the predicted value of $c = 48.39$. My final numerical verification objective was to investigate the variation of this transition point with the parameter v . This requires a precise measure of the transition point, based on loci such as that plotted for period 10^5 in Fig. 6(c). In Fig. 6(d) I show a close-up of this locus around the transition point. This reveals two folds, so for a small range of c values there are three possible solutions with period 10^5 . These folds persist as v is increased, and they are not predicted by my calculations. However, there is no inconsistency, since numerical calculations for a range of v values suggest that the \bar{c} interval between the folds is $o(1)$ as $v \rightarrow \infty$, implying that the fold locations coincide in a single point to leading order as $v \rightarrow \infty$.

A natural numerical measure of the point of transition between the two $\min(U)$ values would be the average of the two fold locations. However, this proves difficult to implement in practice. As v is increased, the value of the period required to effectively approximate the loci of homoclinic solutions also increases. For example, for $v = 10^5$ a period of 10^5 is inadequate, but a period of 10^6 is sufficient. However for such a large value of the period, I have been unable to numerically continue the solution loci around

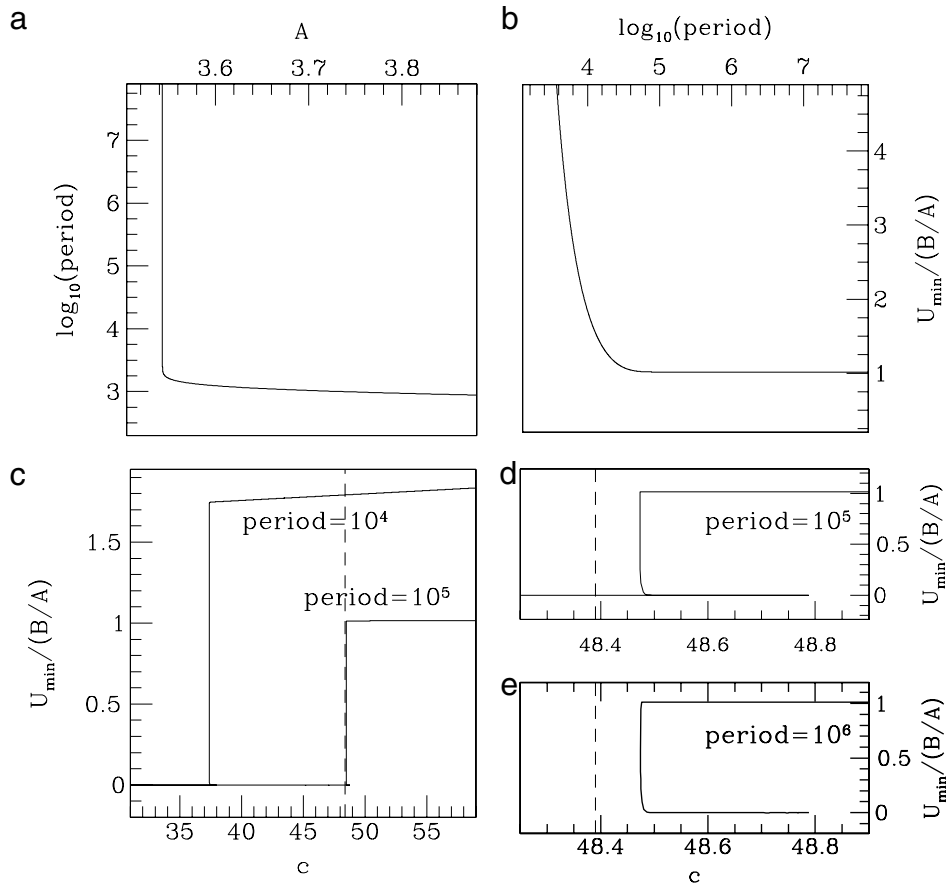


Fig. 6. Numerical verification of the analytical results on the transition between the two homoclinic loci. All numerical solutions were performed using AUTO [39–41] for $B = 0.45$ and $\nu = 10^4$. (a) The variation in the solution period with the rainfall parameter A , for wave speed c fixed at 61, showing the approach to the homoclinic solution. Note that this value of c is significantly above that at which the homoclinic loci intersect. (b) Variation of $\min(U)$ with A , again for $c = 61$. I plot the solution period on the horizontal axis. My analysis predicts that $\min(U) \sim B/A$ as $\nu \rightarrow \infty$ in the infinite period case (i.e. for the homoclinic solution) and this is confirmed by the numerical results. (c) Variation of $\min(U)$ with wave speed c along the loci of solutions of period $= 10^4$ and period $= 10^5$. My analysis predicts an abrupt transition from B/A to zero on the homoclinic solution, to leading order as $\nu \rightarrow \infty$. This is reflected in the numerical solutions for period $= 10^5$ but not for period $= 10^4$. (d) Details of the locus of solutions of period $= 10^5$ around the transition point in $\min(U)$. This shows that the transition is not monotonic in c ; rather, there are two folds. (e) The same plot as in (d), but for period $= 10^6$. The part of the locus shown is almost indistinguishable from that in (d), but there is a convergence failure in numerical continuation close to the second fold. I have been unable to overcome this convergence failure despite large increases in the number of mesh intervals and large decreases in step size. The dashed vertical lines in (c), (d), (e) indicate the leading order approximation to the transition point, which is $\nu^{1/2}\bar{c}_{\text{crit}} = (\sigma^*/\delta^*)^{1/2}B^{3/4}\nu^{1/2}$.

both folds. For example, Fig. 6e illustrates an attempt to perform such a numerical continuation for $\nu = 10^4$ and period $= 10^6$; the locus is almost indistinguishable from that for period $= 10^5$ except that continuation fails close to the fold at $c \approx 48.8$. Changing computational parameters such as the number of mesh intervals enables continuation to proceed a little further, but the convergence failure persists. Therefore an alternative measure of the transition point is required, and I use the value of c at which $\min(U) = \frac{2}{3}(B/A)$, which I denote by c_{num} ; the factor of $2/3$ is chosen because this point can be reached without numerical convergence failure for values of ν up to and including 10^5 , but it is otherwise arbitrary. Fig. 7 illustrates the variation of $c_{\text{num}}/\nu^{1/2}$ with ν , again for $B = 0.45$, demonstrating convergence to the analytically predicted value of 48.39.

6. Discussion

A key ecological issue for vegetation patterns is how they are affected by changes in rainfall. Therefore an important implication of my results is the prediction of a sudden change in solution form as the parameter grouping $\sigma = Ac^{1/2}/(B^{3/2}\nu)$ passes through σ^* . This critical value separates regions I and III of the \bar{A} - \bar{c} plane (see Fig. 3). Although the predicted transition point will only be quantitatively accurate at very large values of ν , the sudden change

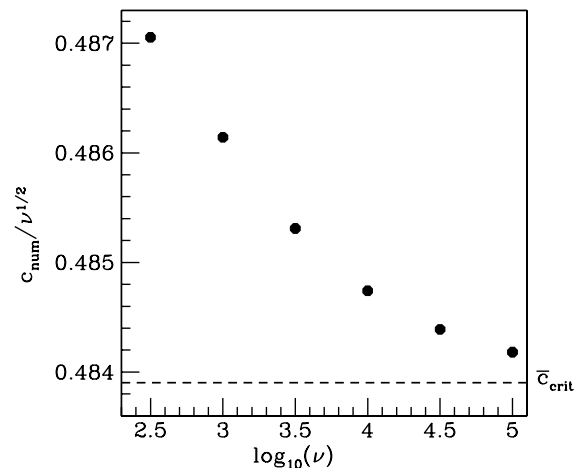


Fig. 7. Numerical verification of the formula that I have derived for \bar{c}_{crit} , which is the point at which the homoclinic solution of (2) changes from being homoclinic to (u_h, w_h) to being homoclinic to $(0, A)$. The value c_{num} was calculated as described in the main text: briefly, it is the value of c at which the minimum of U on solutions of very large fixed period is equal to $\frac{2}{3}(B/A)$. The numerical solutions were performed using AUTO [39–41]. The dashed line indicates the value of \bar{c}_{crit} for this value of B , which is $B = 0.45$. I used 10^7 as the fixed value of the period for all the computations in this figure; the basis on which this value is chosen is described in the main text. Note that this is the period for the unscaled coordinate z , not the scaled coordinate \bar{z} .

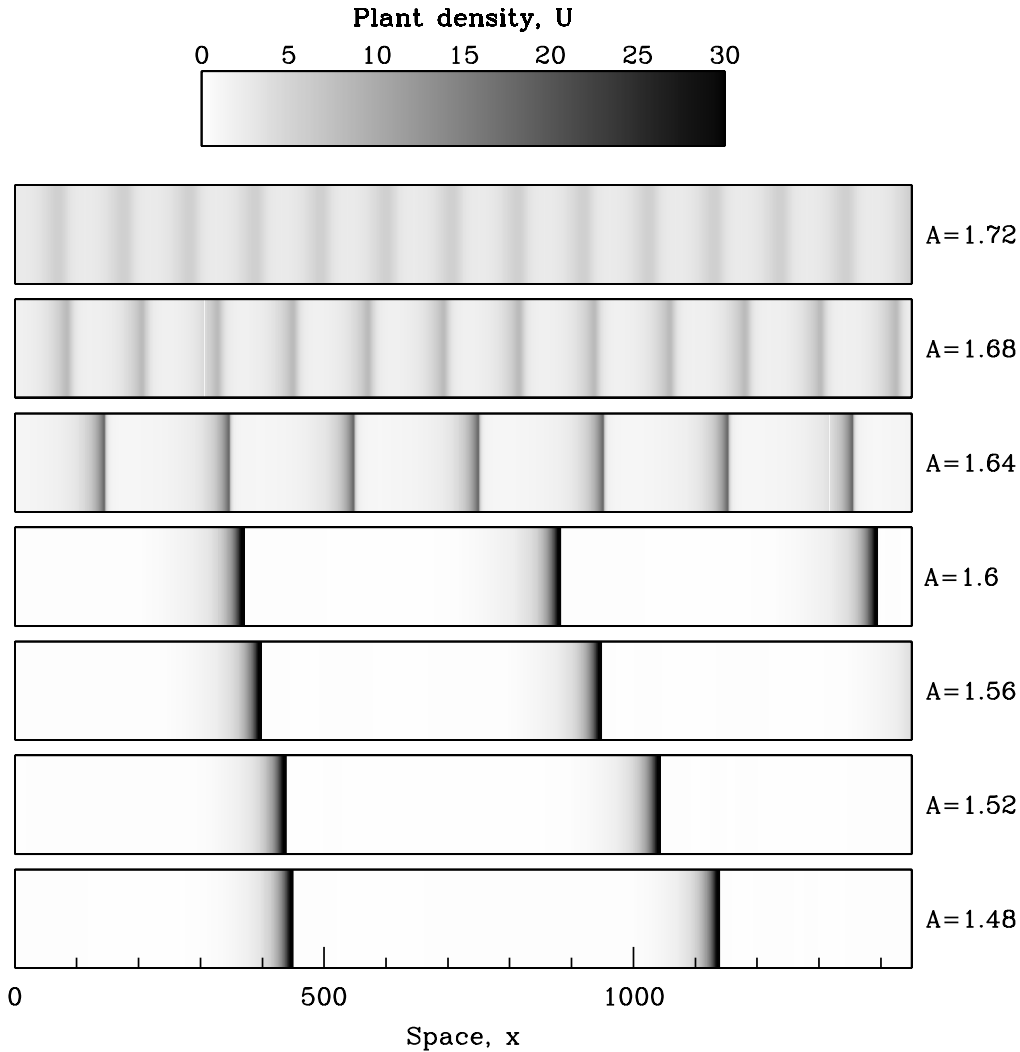


Fig. 8. An illustration of the rapid change in solution form as the rainfall parameter A is decreased. The solutions shown are for wave speed $c = 6.6$, with $B = 0.45$ and $\nu = 200$; note that the same values of the latter two parameters were used in Fig. 1. For these parameter values, patterns occur for values of A between 1.745 (the Hopf bifurcation point) and 1.409 (the homoclinic solution). The plots show the plant density U via greyscale shading. For the largest four values of A , the plant density actually exceeds the upper limit on the scale bar, reaching about $U = 40$ in the vegetation stripes; black shading is used for these values. The solutions were obtained by numerical continuation of (2) as A is varied along the limit cycle branch starting from the Hopf bifurcation point; the numerical continuation was performed using AUTO [39–41].

in pattern form is reflected in numerical solutions of (2) at much lower values. Fig. 8 shows an example of this. As the rainfall parameter A is decreased there is a sharp transition from diffuse patterns of relatively low amplitude, to much more localised patterns with higher plant density. The transition is accompanied by a marked increase in pattern wavelength.

From a mathematical viewpoint, an important and unresolved mathematical issue is the way in which the homoclinic solution changes form in the \tilde{U} - \tilde{W} plane as one moves along the homoclinic loci close to the critical point $A = \sigma^{*3/4} \delta^{*1/4} B^{9/8} \nu^{1/4} c = \sigma^{*1/2} \delta^{*-1/2} B^{3/4} \nu^{1/2}$. As discussed in Section 5, my analysis predicts that at this critical point there is a sudden switch in the minimum value of U on the homoclinic solution, from B/A to zero. However, since solutions of (2) vary continuously with parameters, the minimum value must actually change continuously, and Fig. 6(d) shows an example of this change, calculated numerically. The resolution of this apparent inconsistency is that the region II solution constructed in Section 3 breaks down when $\bar{c} = \bar{c}_{\text{crit}} + o(1)$ as $\nu \rightarrow \infty$. I will now give an intuitive explanation of this breakdown, although I will not attempt to investigate analytically the transition in the minimum value of U : this is a natural area for future work.

A key building block of the solution constructed in Section 3 is the heteroclinic connection between $(P, Q) = (0, 1)$ and $(P, Q) = (1, 0)$ in Eqs. (18). For $\delta < \delta^*$, Proposition 3 shows that this heteroclinic connection approaches $(0, 1)$ algebraically in Z . For δ close to (and below) δ^* , the form of the connection in the P - Q phase plane near $(0, 1)$ is that it has an exponential approach to a point on the centre manifold, which I denote by $(\xi, 1 - \xi)$ (illustrated in Fig. 9; recall that the linear part of the centre manifold is $P + Q = 1$). Thereafter the trajectory follows the centre manifold (approximately) to the steady state $(0, 1)$. Therefore $\xi \rightarrow 0$ as $\delta \rightarrow \delta^{*-}$, and numerical solutions suggest that $\xi = O_s(\delta^* - \delta)$. (Recall that $\delta = k_4 \sigma B^{3/2} / \bar{c}^2$: see the proof of Proposition 3.)

Consider now a point (\bar{A}, \bar{c}) on the homoclinic locus with $\bar{c} > \bar{c}_{\text{crit}}$. The matching conditions in Section 3.6 (with $\zeta = \infty$) imply that the associated value of δ is $\bar{A} / \bar{c}^{3/2}$, which will be $< \delta^*$. If one then considers $\epsilon \rightarrow 0$ (i.e. $\nu \rightarrow \infty$) with \bar{c} fixed at this value, the solution constructed in Section 3 will be valid. But if instead one allows $\bar{c} \rightarrow \bar{c}_{\text{crit}}$ as $\epsilon \rightarrow 0$, the situation is different. In particular, if \bar{c} varies such that $\xi = o(\epsilon)$, then the algebraic approach of (P, Q) to $(0, 1)$ is restricted to values of P that are $o(\epsilon)$, and this prevents matching between \tilde{U}_4 and \tilde{U}_1 . It follows that the solution

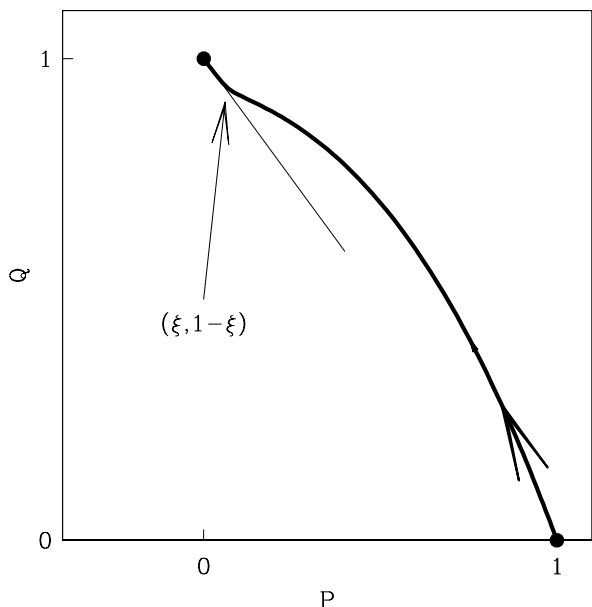


Fig. 9. The form of the heteroclinic connection $\widehat{\Gamma}$ between $(1, 0)$ and $(0, 1)$ in Eqs. (18) for δ just below δ^* . The thick line is the trajectory and the thin line is $P+Q=1$, which is the linearised part of the centre manifold at $(0, 1)$. I define $(\xi, 1-\xi)$ as the point on $P+Q=1$ to which $\widehat{\Gamma}$ has exponential approach. The solution plotted is for $\delta=1.0$, which compares with $\delta^*=1.16$.

structure developed in Section 3 becomes invalid on a part of the homoclinic locus with $0 < \bar{c} - \bar{c}_{\text{crit}} = o(1)$ as $\epsilon \rightarrow 0$ (i.e. as $\nu \rightarrow \infty$). Calculation of the solution structure in this region is a natural objective for future work, and the resulting solution must reflect the decrease in the minimum value of U on the homoclinic region, from u_u to 0. Similarly on the homoclinic locus bordering region III, the homoclinic solution must approach (u_u, w_u) as $\bar{c} \rightarrow \bar{c}_{\text{crit}}$, but I have not investigated the details of this approach.

Acknowledgement

This work was supported in part by a Leverhulme Trust Research Fellowship.

References

[1] C. Valentin, J.M. d'Herbès, J. Poesen, Soil and water components of banded vegetation patterns, *Catena* 37 (1999) 1–24.
 [2] M. Rietkerk, S.C. Dekker, P.C. de Ruiter, J. van de Koppel, Self-organized patchiness and catastrophic shifts in ecosystems, *Science* 305 (2004) 1926–1929.
 [3] D.L. Dunkerley, K.J. Brown, Oblique vegetation banding in the Australian arid zone: implications for theories of pattern evolution and maintenance, *J. Arid. Environ.* 52 (2002) 163–181.
 [4] S.S. Berg, D.L. Dunkerley, Patterned mulga near Alice Springs, central Australia, and the potential threat of firewood collection on this vegetation community, *J. Arid. Environ.* 59 (2004) 313–350.
 [5] C. Montaña, The colonization of bare areas in two-phase mosaics of an arid ecosystem, *J. Ecol.* 80 (1992) 315–327.
 [6] A.K. McDonald, R.J. Kinucan, L.E. Loomis, Ecohydrological interactions within banded vegetation in the northeastern Chihuahuan Desert, USA, *Ecohydrology* 2 (2009) 66–71.
 [7] W. MacFadyen, Vegetation patterns in the semi-desert plains of British Somaliland, *Geogr. J.* 115 (1950) 199–211.
 [8] C. Valentin, J.M. d'Herbès, Niger tiger bush as a natural water harvesting system, *Catena* 37 (1999) 231–256.
 [9] P. Couteron, A. Mahamane, P. Ouedraogo, J. Seghieri, Differences between banded thickets (tiger bush) at two sites in West Africa, *J. Veg. Sci.* 11 (2000) 321–328.
 [10] F. Borgogno, P. D'Odorico, F. Laio, L. Ridolfi, Mathematical models of vegetation pattern formation in ecohydrology, *Rev. Geophys.* 47 (2009) Art. No. RG1005.
 [11] R. Lefever, O. Lejeune, On the origin of tiger bush, *Bull. Math. Biol.* 59 (1997) 263–294.
 [12] P. Couteron, O. Lejeune, Periodic spotted patterns in semi-arid vegetation explained by a propagation-inhibition model, *J. Ecol.* 89 (2001) 616–628.

[13] N. Barbier, P. Couteron, R. Lefever, V. Deblauwe, O. Lejeune, Spatial decoupling of facilitation, competition at the origin of gapped vegetation patterns, *Ecology* 89 (2008) 1521–1531.
 [14] R. Lefever, N. Barbier, P. Couteron, O. Lejeune, Deeply gapped vegetation patterns: on crown/root allometry, criticality and desertification, *J. Theoret. Biol.* 261 (2009) 194–209.
 [15] J.M. Thiéry, J.-M. D'Herbès, C. Valentin, A model simulating the genesis of banded vegetation patterns in Niger, *J. Ecol.* 83 (1995) 497–507.
 [16] A. Mauchamp, S. Rambal, J. Lepart, Simulating the dynamics of a vegetation mosaic: a spatialized functional model, *Ecol. Modell.* 71 (1994) 107–130.
 [17] D.L. Dunkerley, Banded vegetation: development under uniform rainfall from a simple cellular automaton model, *Plant Ecol.* 129 (1997) 103–111.
 [18] C.A. Klausmeier, Regular and irregular patterns in semiarid vegetation, *Science* 284 (1999) 1826–1828.
 [19] J.A. Sherratt, An analysis of vegetation stripe formation in semi-arid landscapes, *J. Math. Biol.* 51 (2005) 183–197.
 [20] R. HilleRisLambers, M. Rietkerk, F. van de Bosch, H.H.T. Prins, H. de Kroon, Vegetation pattern formation in semi-arid grazing systems, *Ecology* 82 (2001) 50–61.
 [21] J. von Hardenberg, E. Meron, M. Shachak, Y. Zarmi, Diversity of vegetation patterns and desertification, *Phys. Rev. Lett.* 87 (2001) Art. No. 198101.
 [22] M. Rietkerk, M.C. Boerlijst, F. van Langevelde, R. HilleRisLambers, J. van de Koppel, H.H.T. Prins, A. de Roos, Self-organisation of vegetation in arid ecosystems, *Am. Nat.* 160 (2002) 524–530.
 [23] E. Gilad, J. von Hardenberg, A. Provenzale, M. Shachak, E. Meron, A mathematical model of plants as ecosystem engineers, *J. Theoret. Biol.* 244 (2007) 680–691.
 [24] N. Ursino, Modeling banded vegetation patterns in semiarid regions: inter-dependence between biomass growth rate and relevant hydrological processes, *Water Resour. Res.* 43 (2007) W04412.
 [25] N. Ursino, Above and below ground biomass patterns in arid lands, *Ecol. Modell.* 220 (2009) 1411–1418.
 [26] G.-Q. Sun, Z. Jin, Q. Tan, Measurement of self-organization in arid ecosystems, *J. Biol. Syst.* 18 (2010) 495–508.
 [27] N. Ursino, S. Contarini, Stability of banded vegetation patterns under seasonal rainfall and limited soil moisture storage capacity, *Adv. Water Resour.* 29 (2006) 1556–1564.
 [28] V. Guttal, C. Jayaprakash, Self-organisation and productivity in semi-arid ecosystems: implications of seasonality in rainfall, *J. Theoret. Biol.* 248 (2007) 290–500.
 [29] A.Y. Kletter, J. von Hardenberg, E. Meron, A. Provenzale, Patterned vegetation and rainfall intermittency, *J. Theoret. Biol.* 256 (2009) 574–583.
 [30] J. van de Koppel, M. Rietkerk, F. van Langevelde, L. Kumar, C.A. Klausmeier, J.M. Fryxell, J.W. Hearne, J. van Andel, N. de Ridder, M.A. Skidmore, L. Stroosnijder, H.H.T. Prins, Spatial heterogeneity and irreversible vegetation change in semiarid grazing systems, *Am. Nat.* 159 (2002) 209–218.
 [31] Y. Pueyo, S. Kefi, C.L. Alados, M. Rietkerk, Dispersal strategies and spatial organization of vegetation in arid ecosystems, *Oikos* 117 (2008) 1522–1532.
 [32] S. Kefi, M. Rietkerk, G.G. Katul, Vegetation pattern shift as a result of rising atmospheric CO₂ in arid ecosystems, *Theor. Popul. Biol.* 74 (2008) 332–344.
 [33] V. Deblauwe, Modulation des structures de végétation auto-organisées en milieu aride/Self-organized vegetation pattern modulation in arid climates, Ph.D. Thesis, Université Libre de Bruxelles, 2010. <http://theses.ulb.ac.be/ETD-db/collection/available/ULBetd-04122010-093151/>.
 [34] D.J. Tongway, J.A. Ludwig, Theories on the origins, maintenance, dynamics, and functioning of banded landscapes, in: D.J. Tongway, C. Valentin, J. Seghieri (Eds.), *Banded Vegetation Patterning in Arid and Semi-Arid Environments*, Springer, New York, 2001, pp. 20–31.
 [35] C. Montaña, J. Seghieri, A. Cornet, Vegetation dynamics: recruitment, regeneration in two-phase mosaics, in: D.J. Tongway, C. Valentin, J. Seghieri (Eds.), *Banded Vegetation Patterning in Arid and Semi-Arid Environments*, Springer, New York, 2001, pp. 132–145.
 [36] A.I. Borthagaray, M.A. Fuentes, P.A. Marquet, Vegetation pattern formation in a fog-dependent ecosystem, *J. Theoret. Biol.* 265 (2010) 18–26.
 [37] J.A. Sherratt, G.J. Lord, Nonlinear dynamics, pattern bifurcations in a model for vegetation stripes in semi-arid environments, *Theor. Popul. Biol.* 71 (2007) 1–11.
 [38] J.A. Sherratt, Pattern solutions of the Klausmeier model for banded vegetation in semi-arid environments I: patterns with the largest possible propagation speeds, *Proc. R. Soc. Lond. Ser. A* 467 (2011) 3272–3294.
 [39] E.J. Doedel, AUTO, a program for the automatic bifurcation analysis of autonomous systems, *Congr. Numer.* 30 (1981) 265–384.
 [40] E.J. Doedel, H.B. Keller, J.P. Kernévez, Numerical analysis and control of bifurcation problems: (I) bifurcation in finite dimensions, *Internat. J. Bifur. Chaos* 1 (1991) 493–520.
 [41] E.J. Doedel, W. Govaerts, Y.A. Kuznetsov, A. Dhooge, Numerical continuation of branch points of equilibria and periodic orbits, in: E.J. Doedel, G. Domokos, I.G. Kevrekidis (Eds.), *Modelling and Computations in Dynamical Systems*, World Scientific, 2006, pp. 145–164.
 [42] J.A. Sherratt, Pattern solutions of the Klausmeier model for banded vegetation in semi-arid environments I, *Nonlinearity* 23 (2010) 2657–2675.
 [43] A.C. Hindmarsh, Odepack a systematized collection of ODE solvers, in: R.S. Stepleman, et al. (Eds.), *Scientific Computing*, North-Holland, Amsterdam, 1983, pp. 55–64.
 [44] L.R. Petzold, Automatic selection of methods for solving stiff, nonstiff systems of ordinary differential equations, *SIAM J. Sci. Stat. Comput.* 4 (1983) 136–148.